Materials Advances

ROYAL SOCIETY OF CHEMISTRY

PAPER

View Article Online
View Journal | View Issue

Cite this: *Mater. Adv.*, 2026, 7, 3586

ROS-scavenging and oxygen-generating MgMn-LDH integrated smart injectable hydrogel for microenvironment-reprogrammable spinal cord injury repair

Lian Ren,†[ab] Xiaobin Zhou,[a] Longbao Feng[d] and Guodong Sun *[ac]

Spinal cord injury (SCI) induces the formation of a complex pathological microenvironment characterized by excessive reactive oxygen species (ROS) accumulation, persistent hypoxia and severe inflammatory responses, which severely impairs the processes of neural regeneration and functional recovery. To address these critical issues, we constructed a hydrogel system for the synergistic repair of SCI by integrating magnesium-manganese layered double hydroxides (MgMn-LDHs) into a ROS/pH-responsive GelMA-PBA/HA-DA hydrogel matrix. Harnessing the redox activity of Mn^{3+}, MgMn-LDHs efficiently scavenge excess ROS and create a regenerative microenvironment favorable for neural repair. Meanwhile, Mg^{2+} promotes axonal elongation, myelination and the polarization of anti-inflammatory M2 macrophages by regulating key neural differentiation signaling pathways. The GelMA-PBA/HA-DA hydrogel, crosslinked *via* dynamic boronate ester bonds, enables the precise and controlled release of MgMn-LDHs in the acidic and highly oxidative pathological microenvironment post-SCI. *In vitro* experiments demonstrated that this hydrogel system could effectively support the proliferation and neurite outgrowth of PC12 cells under hypoxic and ROS-enriched conditions, inhibit the secretion of pro-inflammatory cytokines, and significantly promote vascular regeneration. *In vivo* studies in a mouse SCI model revealed that the hydrogel system markedly improved locomotor function, reduced the expression levels of inflammatory markers, ameliorated the inflammatory status of injured tissues, and effectively facilitated axonal regeneration and remyelination at the injury site. This MgMn-LDHs-loaded GelMA-PBA/HA-DA hydrogel system establishes a multifunctional and translatable therapeutic platform for SCI treatment, and also provides valuable insights for the research on therapeutic strategies against other neurodegenerative diseases.

Received 23rd January 2026,
Accepted 16th February 2026

DOI: 10.1039/d6ma00108d

rsc.li/materials-advances

1. Introduction

Spinal cord injury (SCI) is a severe neurological trauma that often leads to permanent motor and sensory dysfunction, creating a heavy medical and economic burden on patients and society.[1,2] The mortality rate among patients with complete spinal cord injury is as high as 25% to 50%, and this figure rises further to 49–68.8% in patients with high-level complete paraplegia, underscoring the extreme severity of this condition.[3] Currently, clinical treatment strategies mainly focus on surgical decompression, spinal stabilization, and rehabilitation training.[4,5] Although these strategies can improve the quality of life of patients to a certain extent, they fail to fundamentally address the core challenge of neural regeneration.[6]

The pathological progression following SCI can be divided into primary injury and secondary injury.[7] Among these, the cascade reaction induced by secondary injury is the key driver of sustained deterioration in neurological function, with its core features including intense oxidative stress, severe local hypoxia, and neuroinflammation.[8] Excessive reactive oxygen species (ROS) generated post-injury trigger lipid peroxidation, protein/DNA damage, and subsequently induce the apoptosis of neurons and oligodendrocytes, thereby impeding myelination.[9,10] Concurrently, the disruption of vascular

[a] *Guangdong Provincial Key Laboratory of Spine and Spinal Cord Reconstruction, The Fifth Affiliated Hospital of Jinan University (Heyuan Shenhe People's Hospital), Jinan University, Heyuan, 517000, China. E-mail: sgd96@jnu.edu.cn*
[b] *Department of Orthopedic Surgery, Loudi Central Hospital, Loudi, 417000, Hunan Province, China*
[c] *The First Affiliated Hospital of Jinan University, Guangzhou, 510630, China*
[d] *Key Laboratory of Biomaterials of Guangdong Higher Education Institutes, Key Laboratory of Regenerative Medicine of Ministry of Education, Guangdong Provincial Engineering and Technological Research Centre for Drug Carrier Development, Department of Biomedical Engineering, Jinan University, Guangzhou, 510632, China*
† These authors contributed equally to this work.

structures leads to local circulatory disorders, creating a persistent hypoxic microenvironment.[11] This not only exacerbates cell death but also inhibits the differentiation of endogenous neural stem cells and axonal elongation.[12] More critically, hypoxia and ROS further activate and amplify neuroinflammation, while the inflammatory response in turn promotes ROS production, forming a mutually reinforcing vicious cycle.[13,14] Traditional therapeutic approaches primarily aim to modulate the local microenvironment through systemic administration of antioxidants or neurotrophic factors.[15] However, these methods suffer from inherent limitations such as poor targeting, low bioavailability, and short half-lives, resulting in limited therapeutic efficacy that fails to effectively reverse this complex pathological microenvironment.[16] Therefore, the development of novel regenerative medicine strategies capable of actively intervening in the pathological progression of injury and promote a microenvironment favorable for neural regeneration has become one of the most urgent challenges in the current field of neuroscience.

Targeting the pathological microenvironment of SCI, simultaneous elimination of ROS and alleviation of hypoxia is considered one of the most promising therapeutic strategies.[17] In recent years, manganese (Mn)-based nanomaterials have attracted extensive attention. Leveraging the valence-variable property of Mn ions, these materials can efficiently mimic the functions of natural superoxide dismutase (SOD) and catalase (CAT).[18] They catalyze the conversion of superoxide anions ($^{\bullet}O_2^-$) and hydrogen peroxide (H_2O_2) into harmless water and oxygen.[19] While scavenging key ROS, the generated O_2 directly ameliorates the hypoxic environment, laying a foundation for subsequent neural repair.[20] After constructing a beneficial microenvironment with low ROS and high O_2 levels, the active provision of bioactive signals to promote neural regeneration is crucial.[21] Magnesium ions (Mg^{2+}), as an essential intracellular divalent cation, have been proven to possess multiple neuroprotective and reparative functions.[22] They not only directly promote neuronal axon growth and accelerate myelin regeneration but also regulate key signaling pathways like PI3K/Akt to guide neural stem cells toward neuronal differentiation.[23] Layered double hydroxides (LDHs), as biocompatible two-dimensional nanomaterials, exhibit flexible adjustability in interlayer metal composition, making them ideal carriers for constructing such catalytic nanoplatforms.[24,25] Therefore, integrating Mg^{2+} and Mn^{3+} into the same LDH nanostructure to fabricate MgMn-LDH enables the two metal ions to exert a synergistic effect, thereby achieving multi-dimensional and sequential regulation of secondary spinal cord injury. The MgMn-LDH constructed by Chen *et al.* retains excellent bioactive sites. A hydrogel was fabricated *via* hydrogen bonds between ULDH and SF, which promotes the formation of β-sheet structures, endowing the hydrogel with promising potential for the treatment of spinal cord injury (SCI).[26]

However, an ideal delivery system is indispensable for achieving long-term retention and on-demand release of therapeutic agents in the injured microenvironment.[27] Injectable hydrogels are considered ideal local delivery platforms due to their excellent biocompatibility, mechanical properties similar to neural tissue, and ability to perfectly fill the injury cavity.[28–32] Gelatin methacryloyl grafted with phenylboronic acid (GelMA-PBA) exhibits favorable biocompatibility and cell adhesion.[33] More importantly, the boronate ester bonds and acylhydrazone bonds in GelMA-PBA possess dual responsiveness to ROS and pH: they remain stable under conditions of low ROS and neutral pH, but undergo rapid cleavage in the core pathological microenvironment of SCI—characterized by high ROS and acidic Ph.[34,35] This endows the hydrogel with ''smart'' responsive properties, enabling specific and on-demand release of therapeutic drugs at the lesion site, which significantly improves therapeutic efficacy and reduces potential off-target effects. Xu *et al.* fabricated a GelMA-PBA/ChS-DA microgel system loaded with Sanghuang Polysaccharide (SHP) and MXene. This microgel system exhibits pH-responsive and photothermal controlled release properties, effectively promoting the healing of infected wounds and holding great promise as a transformative therapeutic strategy for infected wound repair.[36]

In the present study, we loaded self-developed MgMn-layered double hydroxide (MgMn-LDH) into a ROS/pH dual-responsive smart injectable gelatin methacryloyl-phenylboronic acid/hydroxyapatite-doped alginate (GelMA-PBA/HADA) hydrogel, constructing a synergistic therapeutic platform integrating antioxidant, oxygen supply, and neural regeneration functions (Scheme 1). After local injection, this composite system provides immediate physical support, responds intelligently to the injured microenvironment, and enables precise release of Mg^{2+} and Mn^{3+}. Simultaneously, it efficiently scavenges ROS, generates oxygen *in situ*, and delivers Mg^{2+}-mediated biological signals to promote axonal regeneration and neural differentiation, thereby synergistically reversing the inhibitory microenvironment. Collectively, this work offers a novel and highly translational comprehensive solution for the functional repair of SCI.

2. Materials and method

2.1. Materials

Magnesium nitrate hexahydrate was purchased from J&K Scientific Ltd. (Beijing, China). Manganese nitrate, sodium hydroxide, sodium carbonate, 3-aminophenylboronic acid, and methacrylic anhydride were purchased from Macklin Biochemical Co., Ltd (Shanghai, China). Hydrogen peroxide, hydrochloric acid, xylene, and absolute ethanol were purchased from Sinopharm Chemical Reagent Co., Ltd (China). Gelatin was acquired from Sigma-Aldrich (Shanghai) Trading Co., Ltd (Shanghai, China). Dopamine hydrochloride (DA), *N*-hydroxysuccinimide (NHS) and 1-ethyl-3-(3-dimethylaminopropyl) carbodiimide (EDC) were purchased from Aladdin Reagent (Shanghai) Co., Ltd (Shanghai, China). Fetal bovine serum (FBS), Dulbecco's Modified Eagle Medium (DMEM), and penicillin were obtained from Gibco (USA). The CCK-8 assay kit was

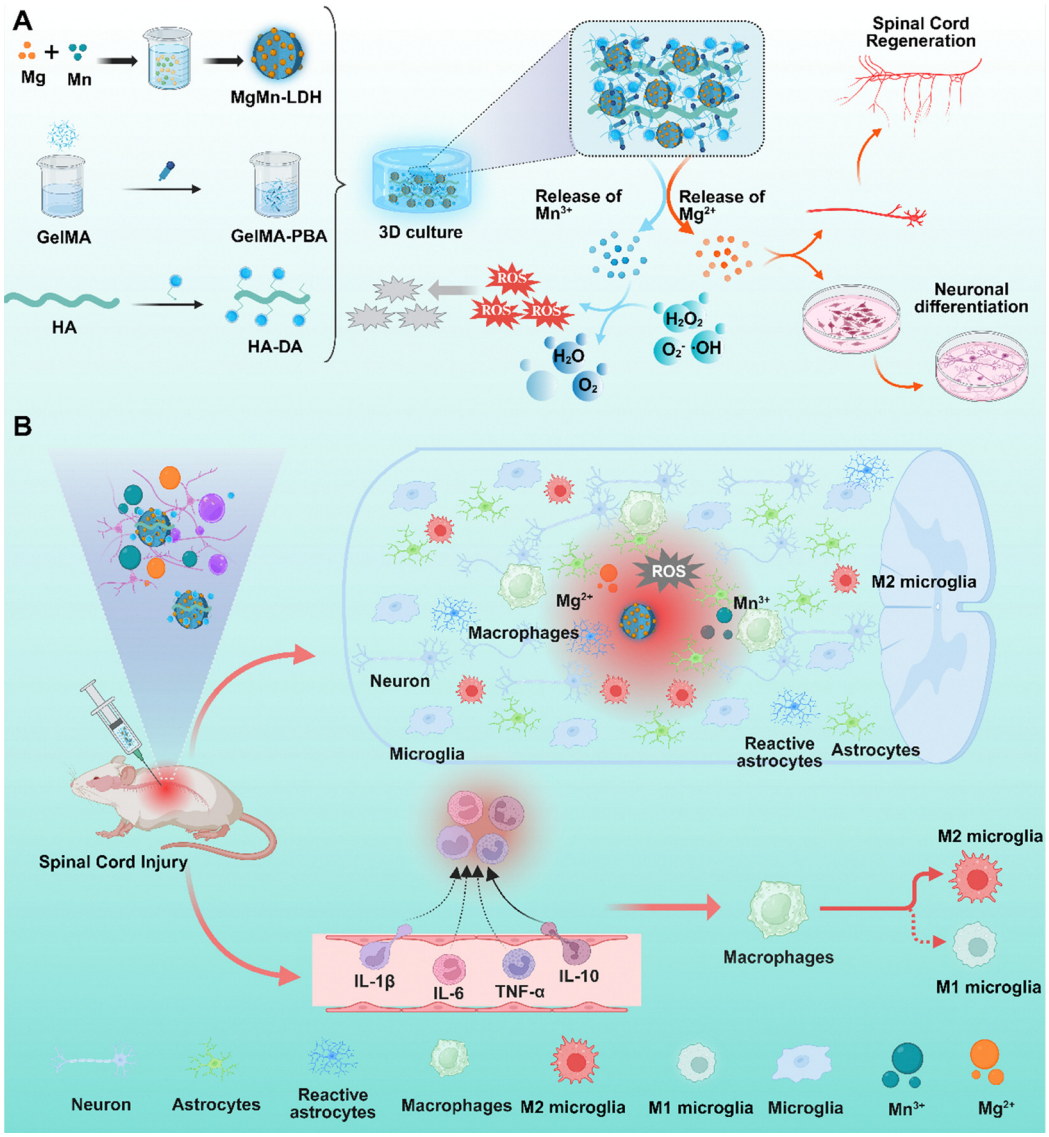

Scheme 1 Scheme of the preparation of MgMn-LDH/GPH hydrogels and the spinal cord injury (SCI) repair process. (A) Preparation process of MgMn-LDH/GPH hydrogels; (B) spinal cord injury (SCI) repair process.

purchased from Beyotime Biotechnology Co., Ltd (Shanghai, China). The DCFH-DA fluorescent probe was acquired from Solarbio (Beijing, China). All antibodies were obtained from Servicebio Technology Co., Ltd (Wuhan, China).

2.2. Materials synthesis

2.2.1. Synthesis of ultrathin MgMn-layered double hydroxide nanosheets (ULDH). Ultrathin MgMn-layered double hydroxide nanosheets (ULDH) were synthesized by an oxidative co-precipitation method. Specifically, Solution A was prepared by dissolving 0.2641 g of $Mg(NO_3)_3{\cdot}6H_3O$ and 0.0573 g of $Mn(NO_3)_2$ in 40 mL of deionized water. Solution B was prepared by dissolving 0.064 g of NaOH, 1.69 mg of Na_2CO_3, and 0.0363 g of 30% (w/w) hydrogen peroxide (H_2O_2) in 40 mL of deionized water. Both solutions were simultaneously added dropwise into a three-necked flask, followed by stirring for 30 minutes to form bulk MgMn-LDH (BLDH). The reaction system was then maintained at 60 °C overnight under a nitrogen (N_2) atmosphere. The resulting BLDH was collected by centrifugation, washed thoroughly with deionized water, and re-dispersed in water to a final concentration of 10 mg mL^{-1}. Subsequently, the BLDH dispersion was mixed with *N*,*N*-dimethylformamide (DMF), and subjected to alternating ultrasonic treatment for 8 hours (0.5 hours per cycle using a cell disruptor and an ultrasonic cleaner, respectively). Un-exfoliated residues were removed by centrifugation; the supernatant was collected, and ULDH was harvested *via* high-speed centrifugation. The obtained ULDH dispersion was stored at 4 °C for subsequent use.

2.2.2. Synthesis of gelatin methacryloyl-phenylboronic acid (GelMA-PBA). 2 g of gelatin was completely dissolved in 50 mL of deionized water at 45 °C. A 50 mL deionized water solution containing 2.4 g of EDC, 2.4 g of NHS, and 1.33 g of

3-aminophenylboronic acid (APBA) was added to the above gelatin solution. The mixture was stirred for 3 days at room temperature, followed by dialysis and freeze-drying to obtain gelatin-phenylboronic acid (Gel-PBA). 1 g of Gel-PBA was fully dissolved in 50 mL of deionized water at 45 °C. Then, 0.6 mL of methacrylic anhydride was added dropwise to the Gel-PBA solution, and the reaction was carried out for 4 h at room temperature. The reaction solution was subjected to dialysis and freeze-drying to obtain gelatin methacryloyl-phenylboronic acid (GelMA-PBA).

2.2.3. Synthesis of hyaluronic acid-dopamine (HA-DA). 1 g of sodium hyaluronate was completely dissolved in 50 mL of deionized water under a nitrogen atmosphere. Then, 575 mg of EDC and 345 mg of NHS were slowly added, and the mixture was stirred for 30 minutes. Subsequently, 569 mg of dopamine hydrochloride was added, and the reaction was carried out for 3 h at room temperature, with the pH of the reaction system maintained at 5–6 during the reaction. Finally, the reaction solution was dialyzed in acidic conditions and freeze-dried to obtain hyaluronic acid-dopamine (HA-DA).

2.2.4. Preparation of GelMA-PBA/HA-DA hydrogel. Gelatin methacryloyl-phenylboronic acid (GelMA-PBA) solutions at concentrations of 5%, 10%, and 15% (w/v) and a hyaluronic acid-dopamine (HA-DA) solution at 10% (w/v) were first prepared separately. Subsequently, GelMA-PBA solutions of different concentrations were mixed with the HA-DA solution at a volume ratio of 1 : 1, and the pH of each mixture was adjusted to 7–8 using 1 M sodium hydroxide (NaOH) solution. After vortexing for thorough mixing, the mixtures were allowed to stand at room temperature to form injectable hydrogels. These hydrogels were designated as 2.5% GPHD, 5.0% GPHD, and 7.5% GPHD, respectively

2.2.5. Preparation of ULDH-loaded GelMA-PBA/HA-DA hydrogel. 2 mg of ULDH were dispersed in 5 mL of 10% (w/v) GelMA-PBA solution. This mixture was then uniformly mixed with 10% (w/v) HA-DA solution at a volume ratio of 1 : 1. The pH of the system was adjusted to 7–8. After vortexing for thorough mixing and subsequent standing, an injectable GPHD@ULDH hydrogel was formed, with a final ULDH concentration of 200 μg mL^{-1}.

2.3. Material characterization

2.3.1. Atomic force microscopy (AFM). BLDH and ULDH nanoparticles were dispersed in deionized water to prepare suspensions with a concentration of 50 μg mL^{-1}. A 10 μL aliquot of each suspension was dropped onto a silicon wafer and air-dried naturally to form a uniform particle distribution. AFM imaging was performed in tapping mode using a silicon probe with a spring constant of approximately 40 N m^{-1} and a resonance frequency of around 300 kHz to minimize sample deformation. The scanning parameters were set below: scanning range of 5 μm × 5 μm, resolution of 512 × 512 pixels, and scanning rate of 1.0 Hz.

2.3.2. High-resolution transmission electron microscopy (HRTEM). BLDH and ULDH nanoparticles were dispersed in deionized water. After ultrasonic dispersion, 20 μL of the solution was dropped onto a copper grid and air-dried naturally. The morphology of the samples was observed using HRTEM with a 5 kV electron beam.

2.3.3. Raman spectroscopy. BLDH and ULDH nanoparticles were placed on a glass slide, which was then transferred to the microscope stage. Optical focusing and secondary laser focusing were performed to optimize photon collection. A 633 nm visible laser was selected, and after switching to this laser, the power was adjusted, followed by setting appropriate integration time and grating size. Raman spectra were recorded in the wavenumber range of 200–1000 cm^{-1} using a Raman spectrometer.

2.3.4. X-ray photoelectron spectroscopy (XPS). The BLDH and ULDH dispersions were drop-cast onto the surface of the substrate and dried in an oven at 55 °C. The dried samples were placed in the sample introduction chamber for vacuum evacuation, and then tested using an X-ray photoelectron spectrometer (XPS).

2.3.5. X-ray diffraction (XRD). BLDH and ULDH nanoparticles were ground into fine powders, then evenly spread in a test dish. The crystal structure of the materials was characterized using an X-ray powder diffractometer. The testing conditions were set as follows: X-ray wavelength = 1.5406 Å, operating voltage = 40 kV, operating current = 40 mA, and scattering angle (2θ) range = 10°–80°.

2.3.6. ^{1}H-NMR. Gelatin (Gel), gelatin-phenylboronic acid (Gel-PBA), gelatin methacryloyl-phenylboronic acid (GelMA-PBA), hyaluronic acid (HA), and hyaluronic acid-dopamine (HA-DA) were dissolved in deuterated water (D_2O) until clear solutions were obtained. The solutions were transferred into clean NMR tubes, and their structures were determined using a nuclear magnetic resonance (NMR) spectrometer at room temperature. The spectra were analyzed using MestReNova software.

2.3.7. Fourier transform infrared spectroscopy (FT-IR). 5 mg of gelatin (Gel), gelatin-phenylboronic acid (Gel-PBA), gelatin methacryloyl-phenylboronic acid (GelMA-PBA), hyaluronic acid (HA), and hyaluronic acid-dopamine (HA-DA) were weighed separately and thoroughly ground with potassium bromide (KBr) powder. The mixtures were pressed into sample pellets under vacuum conditions. Fourier transform infrared (FTIR) spectra were recorded in the range of 4000–400 cm^{-1} using a Fourier transform infrared spectrometer.

2.3.8. Rheological properties. The GPHD microgels were removed from the mold. A 25-millimeter-diameter stainless steel parallel-plate rotor was employed to conduct dynamic strain scanning at room temperature (angular frequency range: 0.1–10 rad s^{-1}) to determine the linear viscoelastic region. The variation curves of the elastic modulus (G') and viscous modulus (G'') were recorded.

2.3.9. Self-healing and injectability. Two pieces of GPHD hydrogel were joined along the edges of their incisions. After standing for 10 minutes, the healed hydrogel was gently pulled with tweezers to evaluate its self-healing performance. The GPHD microgels were loaded into a 1 mL syringe, and the letter "SUE" was written to observe their injectability.

2.3.10. *In vitro* antioxidant properties. $^{\bullet}O_2^-$ scavenging: 0.4 mL of different hydrogels were added to 0.5 mL of Tris-HCl buffer (0.05 mol L^{-1}, pH = 8.2), respectively. After incubation at 25 °C for 20 minutes, 0.1 mL of 10 mmol L^{-1} pyrogallol solution was added. After mixing, the reaction was proceed at 25 °C for 5 minutes. Finally, 0.1 mL of HCl (10 mol L^{-1}) was added to the reaction, and the absorbance curve was measured at wavelengths ranging from 270 nm to 420 nm.

H_2O_2 scavenging: different hydrogels were mixed with 1 mM H_2O_2, and the reaction was proceed in the dark for 30 minutes. After the reaction was completed, a hydrogen peroxide assay kit was used to measure the residual H_2O_2 level in the supernatant, and an ultraviolet-visible (UV-vis) spectrophotometer was employed to detect the absorbance curve at wavelengths ranging from 340 nm to 600 nm.

$^{\bullet}$OH scavenging: different hydrogels were reacted with the precursor solution of the $^{\bullet}$OH scavenging assay kit. After the reaction was completed, the $^{\bullet}$OH scavenging assay kit was used to measure the absorbance of the supernatant, and an ultraviolet-visible (UV-vis) spectrophotometer was employed to detect the absorbance curve at wavelengths ranging from 420 nm to 700 nm.

ABTS scavenging: total antioxidant capacity was measured using the rapid ABTS assay. Antioxidants could inhibit the generation of ABTS$^{\bullet+}$ cation radicals, thereby reducing the absorbance at 414 nm. Absorbance spectra in the wavelength range of 380 nm to 480 nm were recorded using a UV-vis spectrophotometer.

2.3.11. Degradation properties. The hydrogel (GPHD@ULDH) was freeze-dried and weighed, the recorded mass was designated as W_1. The dried hydrogel was then immersed in PBS solutions containing different concentrations of H_2O_2 (0 mM and 50 mM) and PBS solutions with different pH values. The samples were incubated in a constant temperature shaking incubator for 1, 3, 5, 7, 14, and 21 days, respectively. After incubation, the hydrogels were taken out, freeze-dried again, and accurately weighed, with the mass recorded as W_t. The degradation rate (W_r) of the hydrogel was calculated using the following formula:

$$W_r = \frac{W_1 - W_t}{W_1} \times 100\%$$

2.3.12. Determination of dissolved oxygen content. Xanthine (1 mM) and xanthine oxidase (0.016 U mL^{-1}) were reacted at 37 °C for 30 minutes to generate superoxide anions ($^{\bullet}O_2^-$). Subsequently, BLDH and ULDH (200 μg mL^{-1}) were incubated with the obtained $^{\bullet}O_2^-$ solution under stirring, and the amount of dissolved oxygen was monitored using a dissolved oxygen meter. BLDH and ULDH (200 μg mL^{-1}) were incubated with H_2O_2 solution (50 μM) under stirring, and the amount of dissolved oxygen was monitored using a dissolved oxygen meter.

2.3.13. Release of Mg^{2+} and Mn^{3+}. To evaluate the ion release behavior of the hydrogel under different conditions, the cumulative release profiles of Mg^{2+} and Mn^{3+} were measured in oxidative stress and acidic microenvironments, respectively. The hydrogel was incubated in PBS buffer at a constant temperature for release assays. The experimental groups included: control group (pH 7.4, 0 mM H_2O_2),oxidative stress group (pH 7.4, 50 mM H_2O_2), and acidic group (pH 5.5, 0 mM H_2O_2). At predetermined time points, the supernatant was collected for ion concentration detection, and an equal volume of fresh buffer was replenished. The concentrations of Mg^{2+} and Mn^{3+} at different time points were quantified using an inductively coupled plasma optical emission spectrometer (ICP-OES), and the release curves were plotted accordingly.

2.3.14. Scanning electron microscopy (SEM). The freeze-dried hydrogels of different formulations were cut smoothly with a surgical blade. The cross-sections were then fixed onto the sample stage using conductive adhesive, followed by gold sputtering to enhance surface conductivity. The micromorphology of the different hydrogels was observed under SEM.

2.4. Cytological evaluation

2.4.1. CCK-8. The hydrogel extract was prepared by incubating hydrogels with complete DMEM medium at a mass ratio of 1 : 10 at 37 °C for 24 h. C17.2 cells were thawed, resuspended in DMEM, and seeded into 96-well plates at a density of 5000 cells per well, followed by incubation until adherent growth. The medium was then replaced with different hydrogel extracts, and the cells were further cultured for 1, 3, and 5 days. After cultivation, CCK-8 working solution was added for incubation of 30 min, and the absorbance (OD) was measured at a wavelength of 450 nm using a microplate reader. The cell viability was calculated according to the following formula (1):

$$\text{Cell viability}\,(\%) = \frac{\text{OD2} - \text{OD0}}{\text{OD1} - \text{OD0}} \times 100\% \quad (1)$$

where OD2 denoted the OD value of the experimental group, OD1 denoted that of the control group, and OD0 denoted that of the blank.

Among these conditions: normal conditions involved incubation in a constant-temperature CO_2 incubator (with 5% CO_2) at 37 °C. Hypoxic conditions were achieved by sealing the 96-well plate with a GasPak chemical gas-generating pack for 5–10 min, and after the indicator changed color, the sealed bag containing the plate was placed entirely into the incubator for cultivation. For the combined oxidative stress + hypoxic conditions, H_2O_2 was added for co-cultivation on the basis of the hypoxic setup described above.

2.4.2. Live/dead staining. C17.2 cells were thawed, resuspended in DMEM, and seeded into 48-well plates at a density of 10 000 cells per well, followed by incubation until adherent growth. The medium was replaced with different hydrogel extracts for further cultivation of 24 h. After incubation, live/dead staining working solution was added and incubated for 20 min at room temperature. Following washing with PBS, anti-fluorescence quenching agent was added, and images were captured immediately using a fluorescence microscope.

2.4.3. Cellular ROS scavenging. C17.2 cells were thawed, resuspended in DMEM, and seeded into 48-well plates at a

density of 10 000 cells per well, followed by incubation until adherent growth. After treatment with H_2O_2 for 30 min, the medium was replaced with different hydrogel extracts for further cultivation of 24 h. Subsequently, DCFH-DA probe (100 nM) was added and incubated for 20 min at room temperature. After washing, Hoechst 33342 nuclear stain was added and incubated for 20 min at room temperature, and images were captured immediately using a fluorescence microscope.

2.4.4. Cytoskeleton staining. C17.2 cells were thawed, resuspended in DMEM, and seeded into 48-well plates at a density of 10 000 cells per well, followed by incubation until adherent growth. The medium was replaced with different hydrogel extracts for further cultivation of 3 and 5 days. After cultivation, fixative solution, permeabilization buffer, and blocking buffer were sequentially added. Upon completion of these steps, phalloidin working solution and DAPI working solution were added for staining. Finally, the cells were mounted with an anti-fluorescence quencher and immediately imaged using a fluorescence microscope.

2.4.5. Cell migration. C17.2 cells were thawed, resuspended in DMEM, and seeded into 48-well plates at a density of 10 000 cells per well, followed by incubation until adherent growth. The medium was replaced with different hydrogel extracts for further cultivation of 24 h. After treatment with H_2O_2 for 30 min, a scratch was made along the middle of each well. The medium was then replaced with different hydrogel extracts again for continued cultivation. At 0, 4, and 12 h post-scratching, images of the scratch wounds were captured using an optical microscope, and the scratch area was measured to calculate the cell migration rate.

2.4.6. Macrophage polarization. RAW264.7 cells were seeded onto coverslips placed in 6-well plates. After overnight induction with 5 μg mL^{-1} lipopolysaccharide (LPS) to polarize cells into the M1 phenotype, the medium was replaced with different hydrogel extracts for an additional 24 h. Cells were then fixed, permeabilized, and blocked, followed by incubation with primary antibodies against iNOS and CD206. After washing, corresponding fluorescently labeled secondary antibodies were applied. Following secondary antibody incubation, nuclei were counterstained with DAPI. Finally, coverslips were mounted with an anti-fluorescence quenching mounting medium, and images were captured using a fluorescence microscope for subsequent analysis. For flow cytometry, cells were harvested by trypsinization, and the resulting cell suspension was incubated with fluorescently labeled antibodies against CD86 and CD206. After incubation, the percentage of M1 and M2 phenotypes was analyzed using a flow cytometer.

2.4.7. Immunofluorescence staining. PC12 cells were resuscitated, resuspended in DMEM complete medium, and seeded into 6-well plates containing cell coverslips, followed by culture until the cells were adherent. The cells were then incubated with 1 mM H_2O_2 for 30 min, washed, and the medium was replaced with different hydrogel extracts for further culture (3 and 5 days). After permeabilization and blocking, the cells were incubated overnight with primary antibodies against F-actin, MAP-2, and GFAP. The corresponding fluorescently labeled secondary antibody was added and incubate for 60 min at room temperature. Following secondary antibody incubation, nuclei were counterstained with DAPI staining solution. Finally, the coverslips were mounted using an anti-fluorescence quenching mounting medium, and images were captured under a fluorescence microscope.

2.4.8. qPCR. RAW264.7 cells cultured in different hydrogel extracts for 24 h were treated with Trizol reagent, followed by lysis and extraction on ice to obtain total RNA. The RNA was then applied to a gDNA adsorption column for purification, and reverse transcription was performed to synthesize complementary DNA (cDNA). The PCR instrument was programmed with the appropriate reaction protocol, and melting curves and amplification curves were generated *via* instrument detection.

2.5. *In vivo* evaluation

2.5.1. Establishment of the SCI model. The Institutional Animal Care and Use Committee (IACUC) of Ruige Biotechnology granted ethical approval for the animal experiments described herein (Approval No. 20250520-001), and all procedures were carried out in compliance with relevant regulatory requirements and ethical guidelines. Rats were anesthetized and fixed on the operating table. The hair on the back was removed, and the spinal skin was incised with a scalpel to expose the T9-T10 segments of the spinal cord. A rongeur was used to remove the T9-T10 vertebral bodies, and the spinal cord was transected at a 1–2 mm segment. Subsequently, the corresponding hydrogel material was implanted at the injury site. Finally, the incision was sutured and disinfected, and the rats were observed continuously.

2.5.2. BBB scoring. After the establishment of the rat spinal cord injury (SCI) model, the BBB scoring was initiated. In accordance with the scoring criteria, scoring and recording were performed at 0, 7, 14, 28, 35, and 42 days post-modeling.

2.5.3. Animal footprint analysis. At 42 days post-surgery, footprint analysis was conducted on the rats. The forelimbs and hindlimbs of the rats were dyed with red and black ink, respectively. The rats were then placed on white paper to walk in a straight line, and photographs were taken to record the footprint patterns on the white paper for the purpose of evaluating the spinal cord repair efficacy.

2.5.4. H&E staining. Spinal cord tissues were fixed in paraformaldehyde, subjected to gradient dehydration, followed by embedding in paraffin. The tissues were sectioned into slices with a thickness of 4 μm. The slices were flattened on glass slides after dewaxing. The slices were sequentially stained with Harris hematoxylin staining solution and eosin staining solution. After dehydration to transparency, the slices were mounted with coverslips, and images were captured under a light microscope.

2.5.5. Masson staining. Bladder tissues were fixed in paraformaldehyde, subjected to gradient dehydration, followed by embedding in paraffin. The tissues were sectioned into slices with a thickness of 4 μm. The slices were flattened on glass

slides after dewaxing. The slices were sequentially stained with hematoxylin staining solution, Ponceau staining solution, and aniline blue staining solution. After dehydration to transparency, the slices were mounted with coverslips, and images were captured under a light microscope.

2.5.6. Immunofluorescence staining. Spinal cord tissues were fixed in paraformaldehyde, subjected to gradient dehydration, followed by embedding in paraffin. The tissues were sectioned into slices with a thickness of 4 μm. Antigen retrieval and blocking were performed on the tissues after dewaxing. Subsequently, primary antibodies were added for overnight incubation, and after that, fluorescently labeled secondary antibodies corresponding to the primary antibodies were added and incubated at room temperature. After the incubation was completed, DAPI staining solution was added and incubated at room temperature. Finally, anti-fluorescence quenching mounting medium was added for coverslip mounting, and images were captured under a fluorescence microscope.

2.5.7. Western blot. Spinal cord tissues were harvested and placed on ice. RIPA protein lysis buffer was added, followed by grinding and lysis for 1 hour. Protein samples were collected by centrifugation. After high-temperature denaturation of the proteins, the samples were loaded onto the gel for electrophoresis. Following electrophoresis, membrane transfer, antibody incubation, and development, the protein bands were visualized using a developer. Finally, the protein bands were collected and analyzed.

2.6. Statistical analysis

All data were presented as mean ± standard deviation (SD) with at least three parallel replicates per group. Statistical analysis was performed using GraphPad Prism software with one-way analysis of variance (ANOVA), where $*p < 0.05$, $**p < 0.01$, and $***p < 0.001$.

3. Results and discussion

3.1. Structure and composition characterization of ULDH

The bulk MgMn-LDH nanosheets (BLDH) were prepared *via* the oxidation co-precipitation method. Subsequently, ultrathin MgMn-LDH nanosheets (ULDH) were obtained by ultrasonic exfoliation of BLDH (Fig. S1A). Transmission electron microscopy (TEM) further characterized the morphology of the synthesized ULDH. As shown in Fig. 1B, ULDH exhibited a hexagonal sheet-like structure with an average lateral size of approximately 50 nm. The elemental mapping results in Fig. 1A confirmed a uniform distribution of O, Mn, and Mg elements within the ULDH nanosheets. High-resolution TEM (HRTEM) was employed to examine the material's surface, as shown in Fig. 1C, which displayed regularly arranged lattice fringes with an interplanar spacing of approximately 0.18 nm. This spacing corresponded to the characteristic distance of the (015) crystal plane in layered double hydroxide (LDH) structures, indicating that the sample retained the crystalline structure of LDH with good local crystal orientation and order.[37] Fig. 1D presented the EDS elemental distribution of ULDH, showing the presence of O, Mn, and Mg elements, consistent with the mapping results. X-ray diffraction (XRD) patterns of ULDH and BLDH were shown in Fig. 1E. Both samples exhibited well-indexed peaks corresponding to the characteristic (003) and (006) lattice planes (JCPDS No. 33-0869), confirming the successful synthesis of ULDH and the retention of its crystal structure after ultrasonic exfoliation.[37] The Raman spectrum of ULDH, shown in Fig. 1F, exhibited a distinct blue shift, attributed to weak long-range van der Waals interactions within the layered material, indicating enhanced catalytic activity of ULDH. X-ray photoelectron spectroscopy (XPS) results for ULDH, shown in Fig. 1G–I, confirmed the presence of O, Mg, and Mn elements. Notably, compared to BLDH, the XPS spectrum of Mn 2p in ULDH showed a lower binding energy, suggesting the presence of more defect sites in ULDH, which enhanced its catalytic performance. Atomic force microscopy (AFM) images (Fig. 1J–O) revealed that the thickness of BLDH ranges from approximately 3.82 nm to 4.21 nm, while the exfoliated ULDH exhibited a reduced thickness ranging from 2.97 nm to 3.64 nm, indicating a significant decrease in thickness and the exposure of more active sites.[38]

3.2. Structural characterization of hydrogels

During the synthesis of GelMA-PBA, phenylboronic acid was first grafted onto the gelatin backbone *via* an amidation reaction to yield Gel-PBA. Subsequently, methacrylate groups were grafted onto Gel-PBA through an esterification reaction, ultimately producing GelMA-PBA. The ^{1}H NMR spectrum of GelMA-PBA was shown in Fig. 2A, displaying characteristic peaks of the benzene ring from phenylboronic acid at 7.60 and 7.45 ppm, confirming the successful synthesis of Gel-PBA. After methacrylation, characteristic peaks of the vinyl group from methacrylate appeared at 5.53 and 5.31 ppm, indicating the successful synthesis of GelMA-PBA.[36] The ^{1}H NMR spectrum of HA-DA was presented in Fig. 2B, showing a characteristic peak of the catechol group at 7.32 ppm, resulting from the amidation reaction between the carboxyl group of hyaluronic acid and dopamine hydrochloride, thus verifying the successful synthesis of HA-DA.[39] The Fourier transform infrared (FTIR) spectrum of GelMA-PBA was shown in Fig. 2C, exhibiting a strong absorption peak at 1332 cm^{-1} attributed to the B–O stretching vibration after phenylboronic acid grafting.[40] Additionally, the C═C stretching vibration peak at 1636 cm^{-1} served as a typical signature of methacrylation, confirming the successful synthesis of GelMA-PBA. The FTIR spectrum of HA-DA (Fig. 2D) displayed two absorption peaks at 1574 cm^{-1} and 1266 cm^{-1}, ascribed to C═N stretching and aromatic C–C stretching vibrations, respectively, further validating the successful coupling of the DA functional group to the HA backbone.[41] GelMA-PBA and HA-DA crosslink to form a stable hydrogel *via* dynamic boronate ester bonds (Fig. S1B). The gelation process of hydrogels at different concentrations (2.5%, 5%, and 7.5%) was recorded, as shown in Fig. 2E. With increasing concentration, the gelation time shortened significantly. Quantitative results (Fig. 2F) indicated that the 7.5%

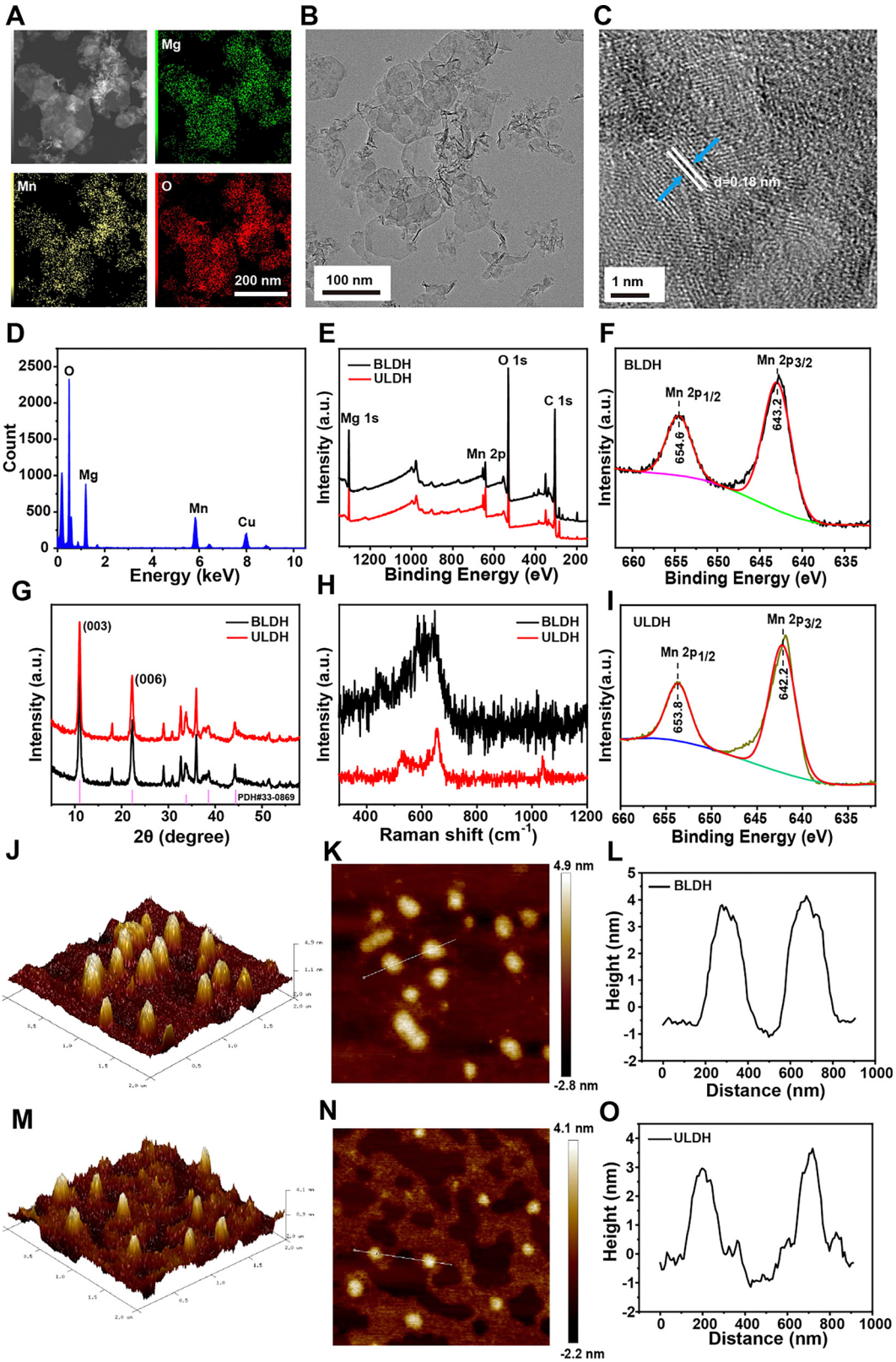

Fig. 1 Composition and Structural Characterization of ULDH. (A) TEM images and elemental distribution of ULDH; (B) high-resolution TEM (HRTEM) images of ULDH; (C) HRTEM images of ULDH; (D) EDS spectra of ULDH; (E) X-ray diffraction (XRD) patterns of ULDH and BLDH; (F) Raman spectrum of ULDH; (G) XPS survey spectra of ULDH and BLDH; (H) high-resolution XPS spectra of Mn for BLDH; (I) high-resolution XPS spectra of Mn for ULDH; (J) 3D height topography AFM images of BLDH; (K) 2D topographic AFM images of BLDH; (L) height profiles and single-sheet thickness of BLDH; (M) 3D height topography AFM images of ULDH; (N) 2D topographic AFM images of ULDH; (O) height profiles and single-sheet thickness of ULDH.

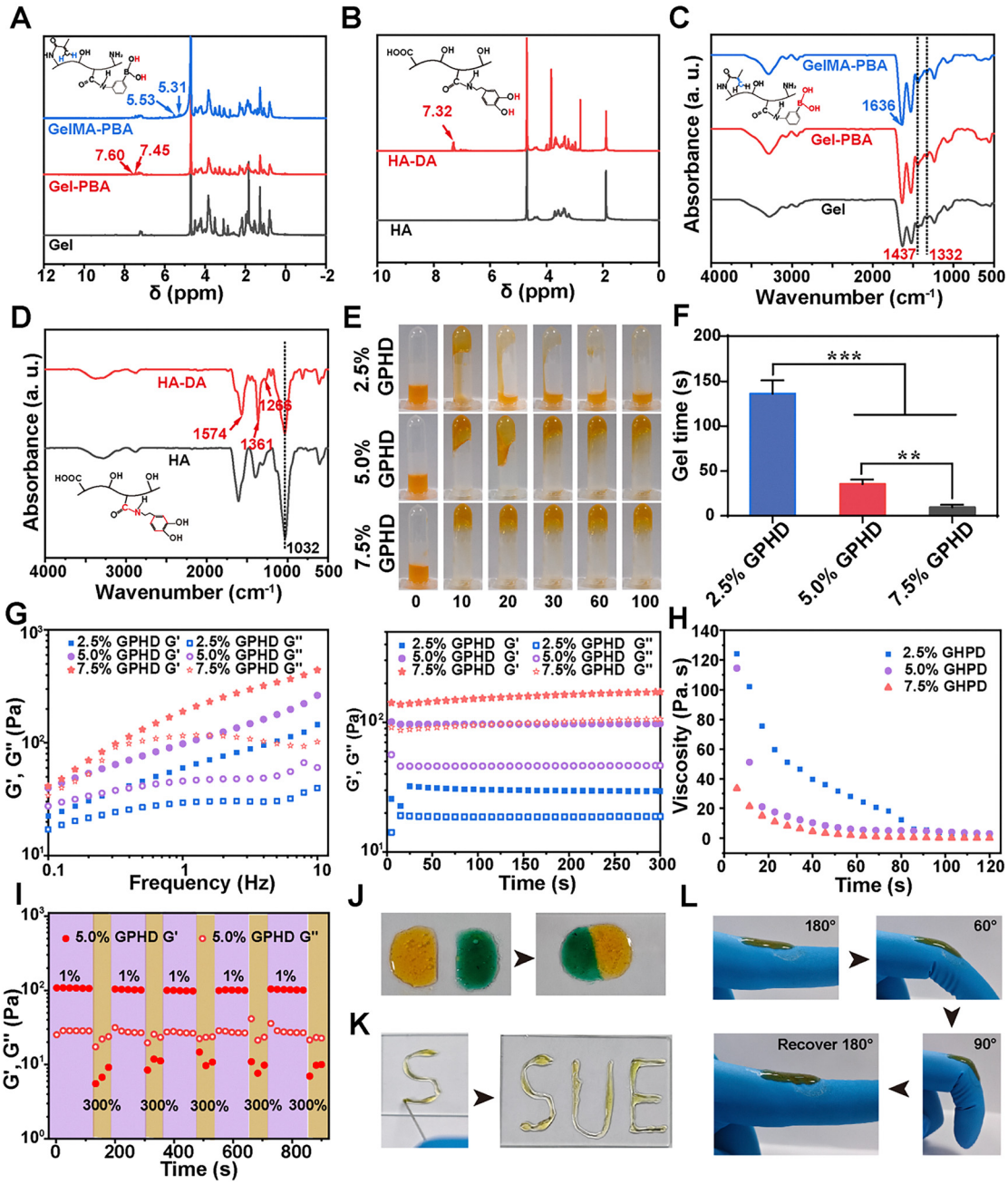

Fig. 2 Preparation and characterization of Gel hydrogels. (A) ^{1}H-Nuclear Magnetic Resonance (^{1}H-NMR) spectra of Gel, Gel-PBA, and GelMA-PBA; (B) ^{1}H-NMR spectra of HA and HA-DA; (C) Fourier transform infrared (FT-IR) spectra of Gel, Gel-PBA, and GelMA-PBA; (D) FT-IR spectra of HA and HA-DA; (E) photographs of the gelation process of hydrogel solutions with different concentrations; (F) statistical plot of the gelation time of hydrogels; (G) rheological frequency sweep curves and time sweep curves of hydrogels with different concentrations; (H) shear viscosity curves; (I) rheological properties of 5% GPHD hydrogel under high and low strains; (J) verification of self-healing properties; (K) injectability of hydrogels; (L) flexibility and adhesion properties of hydrogels under multi-angle bending.

GPHD hydrogel formed rapidly within 10 s, whereas lower concentration groups required longer times to achieve a complete gel state, demonstrating that higher concentrations substantially accelerated the dynamic crosslinking rate of boronate ester bonds. Subsequently, the micromorphology of the different hydrogels was observed by SEM, as shown in Fig. S2. With increasing concentration, the compactness of the internal network structure of the hydrogels was enhanced, which further indicates that the formation of more boronate ester bonds resulted in an increased crosslinking density. Rheological tests were conducted to evaluate the mechanical properties and structural stability of the hydrogels.[42] The results of frequency sweep (Fig. 2G) showed that the storage modulus (G') of hydrogels with different concentrations was higher than the loss modulus (G''), exhibiting typical gel characteristics. This indicated that a stable three-dimensional crosslinked network

structure had been formed inside the hydrogels, endowing them with good elastic bearing capacity. Moreover, with the increase of concentration, the modulus of the hydrogels increased. At higher concentrations, the number of crosslinking sites in the hydrogels increased significantly, leading to a denser three-dimensional network structure formed by the dynamic crosslinking of boronate ester bonds. The interaction between molecular chains was enhanced, and thus the network rigidity and elastic recovery capacity were improved. The results of time sweep test indicated that the modulus of the hydrogels remained stable under shear action, demonstrating excellent structural stability. This stable mechanical property was not derived from rigid crosslinking, but from the rapid reconstruction and balance of the dynamic crosslinked network. This not only ensures structural stability, but also retains a certain degree of flexibility, making it more suitable for the complex *in vivo* tissue environment. Shear viscosity tests (Fig. 2H) demonstrated pronounced shear-thinning behavior, with viscosity decreasing as shear rate increased, facilitating smooth extrusion from syringes and confirming the injectability of the hydrogels. To assess self-healing capability, cyclic tests were performed under alternating 1% and 300% strains, showing rapid recovery of G' after each cycle (Fig. 2I), indicative of the excellent reconstruction ability and network memory of the dynamic boronate ester crosslinking structure.[43] Self-healing experiments (Fig. 2J) further demonstrated that the cut hydrogels spontaneously healed at room temperature, with seamless fusion and no visible cracks. Injectability tests (Fig. 2K) showed that the hydrogels could be extruded smoothly through fine needles to form complex text and patterns (*e.g.*, ''SUE''), confirming superior injectability and moldability. Adhesion evaluation (Fig. 2L) revealed stable attachment of the hydrogels to surfaces at various bending angles without fracture or detachment, highlighting their compliant structure, strong adaptability, and suitability for application on complex tissue surfaces.

3.3. Antioxidant and ROS scavenging evaluation of hydrogels

To evaluate the oxidative stress regulation and environmental responsiveness of the GPHD@ULDH hydrogel, systematic analyses were conducted on its scavenging capabilities for various reactive oxygen species (ROS), dissolved oxygen generation, and stimuli-responsive degradation behavior. Fig. 3A showed the hydroxyl radical ($^{\bullet}OH$) scavenging results. As the ULDH doping concentration increased (10–200 μg mL^{-1}), the degree of decolorization of the characteristic dye significantly intensified, with the absorption peak continuously decreasing, indicating a concentration-dependent $^{\bullet}OH$ scavenging ability. Similarly, in the superoxide anion ($^{\bullet}O_2^-$) scavenging experiment (Fig. 3B), the spectral absorption peak also decreased with increasing ULDH concentration, demonstrating strong $^{\bullet}O_2^-$ scavenging activity. A similar trend was observed for H_2O_2 scavenging (Fig. 3C), indicating that ULDH within the hydrogel effectively decomposes ROS intermediates. The overall antioxidant capacity was validated through the ABTS free radical scavenging assay, as shown in Fig. 3D, where the absorption peak at 420 nm exhibited significant attenuation, further confirming that GPHD@ULDH possesses superior broad-spectrum antioxidant capacity compared to BLDH and the undoped control group. To further investigate the oxygen supply capacity after ROS reaction, changes in dissolved oxygen levels were measured following treatment with H_2O_2 and $^{\bullet}O_2^-$. As shown in Fig. 3E and F, the ULDH group generated significantly higher dissolved oxygen in both ROS systems, reaching up to ~13 ppm after H_2O_2 treatment compared to ~10 ppm for BLDH, with no notable change in the blank control. In the $^{\bullet}O_2^-$ system, ULDH similarly exhibited higher O_2 generation. These results suggested that ULDH not only scavenges ROS but also catalyzed oxygen production, potentially alleviating hypoxic conditions at injury sites and improving the tissue microenvironment.[44] Fig. 3G showed the degradation curves of GPHD@ULDH hydrogels under different H_2O_2 concentrations. The results demonstrated that in a 50 mM H_2O_2 environment, the degradation rate of the hydrogel was significantly accelerated, with almost complete degradation after 21 days. In contrast, the hydrogel remained stable in the absence of H_2O_2, indicating its excellent ROS-responsive property. Fig. 3H further revealed that the degradation rate of the hydrogel in a weakly acidic environment (pH = 5.5) was significantly higher than that at pH = 7.4. Moreover, the hydrogel structure was disrupted at pH = 5.5, demonstrating its acid-responsive capability. This degradation rate aligns with endogenous repair processes, making it highly suitable for SCI repair. Subsequently, the ion release behavior of GPHD@ULDH hydrogels in a simulated pathological microenvironment of SCI high ROS levels and acidic (pH) was evaluated. We investigated the cumulative release rates of Mg^{2+} and Mn^{3+} under different H_2O_2 concentrations and pH values. In acidic environments, protonation of phenylboronic acid (PBA) takes place, leading to the reversible cleavage of boronate ester bonds. In ROS environments, the B–O bonds within the boronate ester linkages are broken, triggering the dissociation of dynamic bonds. Both events cause the relaxation and degradation of the hydrogel network, thereby enabling ROS/pH-responsive drug release. Under H_2O_2 treatment (Fig. 3I), Mg^{2+} release was slow in the absence of H_2O_2, with a cumulative release rate of only 47.7% ± 3.4% at 240 h. When the H_2O_2 concentration was 50 mM, the cumulative release rate increased to 78.0% ± 4.8%, exhibiting a distinct ROS-responsive behavior. Under acidic conditions (Fig. 3J), the cumulative release rate of Mg^{2+} was 72.7% ± 3.0% at pH = 7.4, which increased to 92.5% ± 2.3% when the pH was reduced to 5.5, indicating pH-responsive characteristics. The release profiles of Mn^{3+} under H_2O_2 treatment and pH = 5.5 are presented in Fig. 3K and L. Notably, the release of Mn^{3+} was significantly enhanced in the presence of 50 mM H_2O_2 and at pH = 5.5. These results collectively confirmed that the ion release of the hydrogel was highly dependent on the pathological microenvironmental signals of SCI.[45]

3.4. Evaluation of biocompatibility and ROS-scavenging activity of MgMn-LDH@GPH hydrogels

Excellent biocompatibility was crucial for spinal cord repair materials. To evaluate the cytotoxicity of MgMn-LDH/GPH

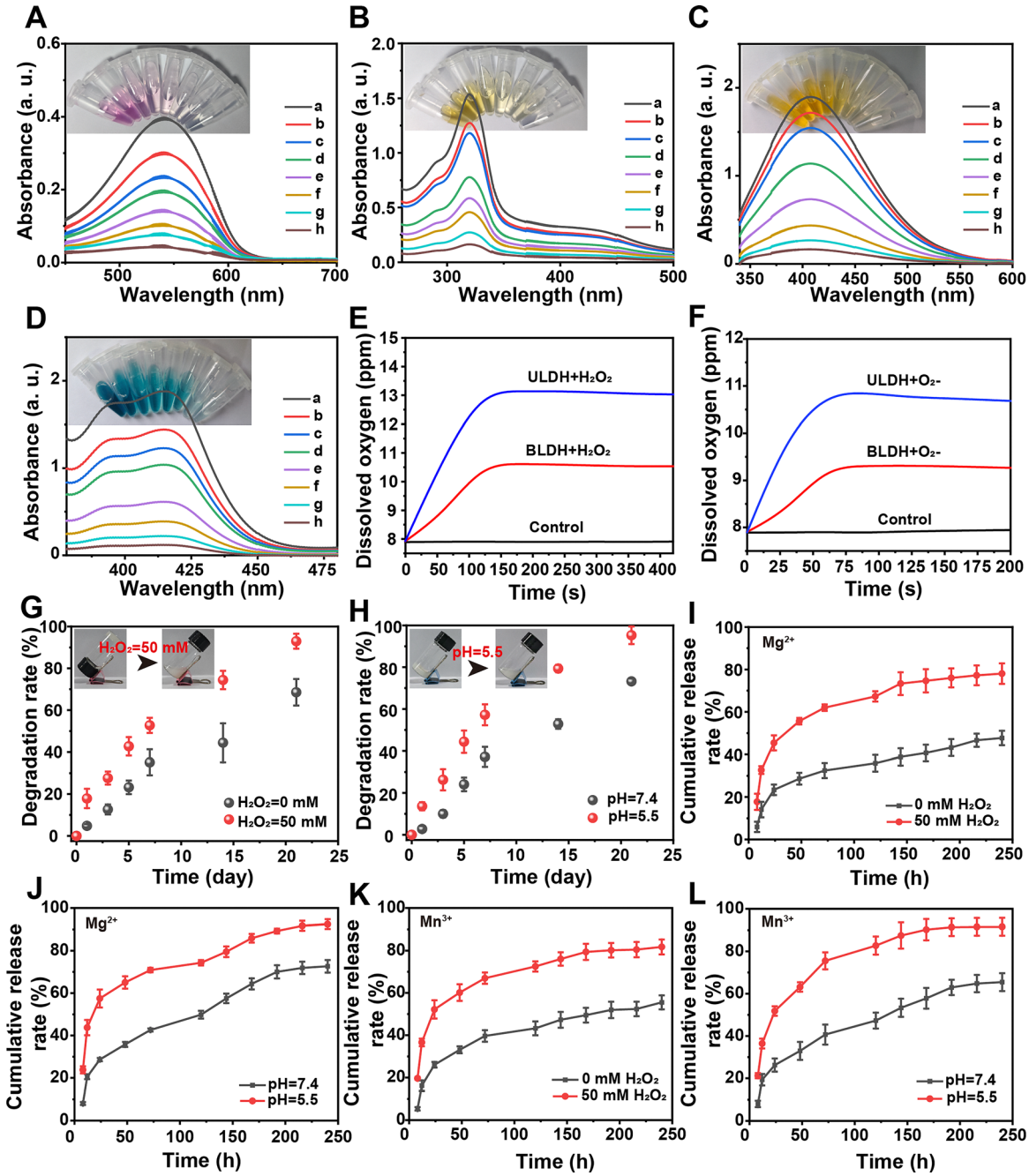

Fig. 3 Antioxidant Activity and Evaluation of ROS Scavenging Capacity of Hydrogels. (A) Evaluation of hydroxyl radical (•OH) scavenging capacity of hydrogels; (B) superoxide anion radical ($^{\bullet}O_2^-$) scavenging capacity of hydrogels; (C) evaluation of hydrogen peroxide (H_2O_2) scavenging capacity of hydrogels; (D) total antioxidant activity of hydrogels characterized by the ABTS method; (E) dissolved oxygen content of BLDH and ULDH in the H_2O_2 system; (F) dissolved oxygen content of BLDH and ULDH in the superoxide anion radical ($^{\bullet}O_2^-$) system; (G) degradation curves of GPHD@ULDH hydrogels under different H_2O_2 concentrations (inset: Image of degradation after 21 days in a 50 mM H_2O_2 environment); (H) Degradation curves of GPHD@ULDH hydrogels under different pH conditions (inset: Image of degradation after 21 days at pH = 5.5); (I and J) Cumulative release rates of Mg^{2+} from GPHD@ULDH hydrogels under different H_2O_2 concentrations and pH values; (K and L) Cumulative release rates of Mn^{3+} from GPHD@ULDH hydrogels under different H_2O_2 concentrations and pH values. (Among Fig. A–D, a to h represent in sequence: control, GPH, GPH@BLDH (BLDH: 50 μg mL^{-1}), GPH@ULDH (ULDH: 10 μg mL^{-1}), GPH@ULDH (ULDH: 25 μg mL^{-1}), GPH@ULDH (ULDH: 50 μg mL^{-1}), GPH@ULDH (ULDH: 100 μg mL^{-1}), GPH@ULDH (ULDH: 200 μg mL^{-1})).

hydrogels in a simulated pathological microenvironment of SCI, we first investigated their effects on the cell viability of mouse neural stem cells (C17.2). CCK-8 assay results showed that under normal conditions (Fig. 4A), the cell viability of the control group was close to 100%, while that of the MgMn-LDH/GPH group, although slightly decreased, remained above 85%, indicating the favorable biocompatibility of MgMn-LDH/GPH hydrogels. Under hypoxic conditions (Fig. 4B), the viability of

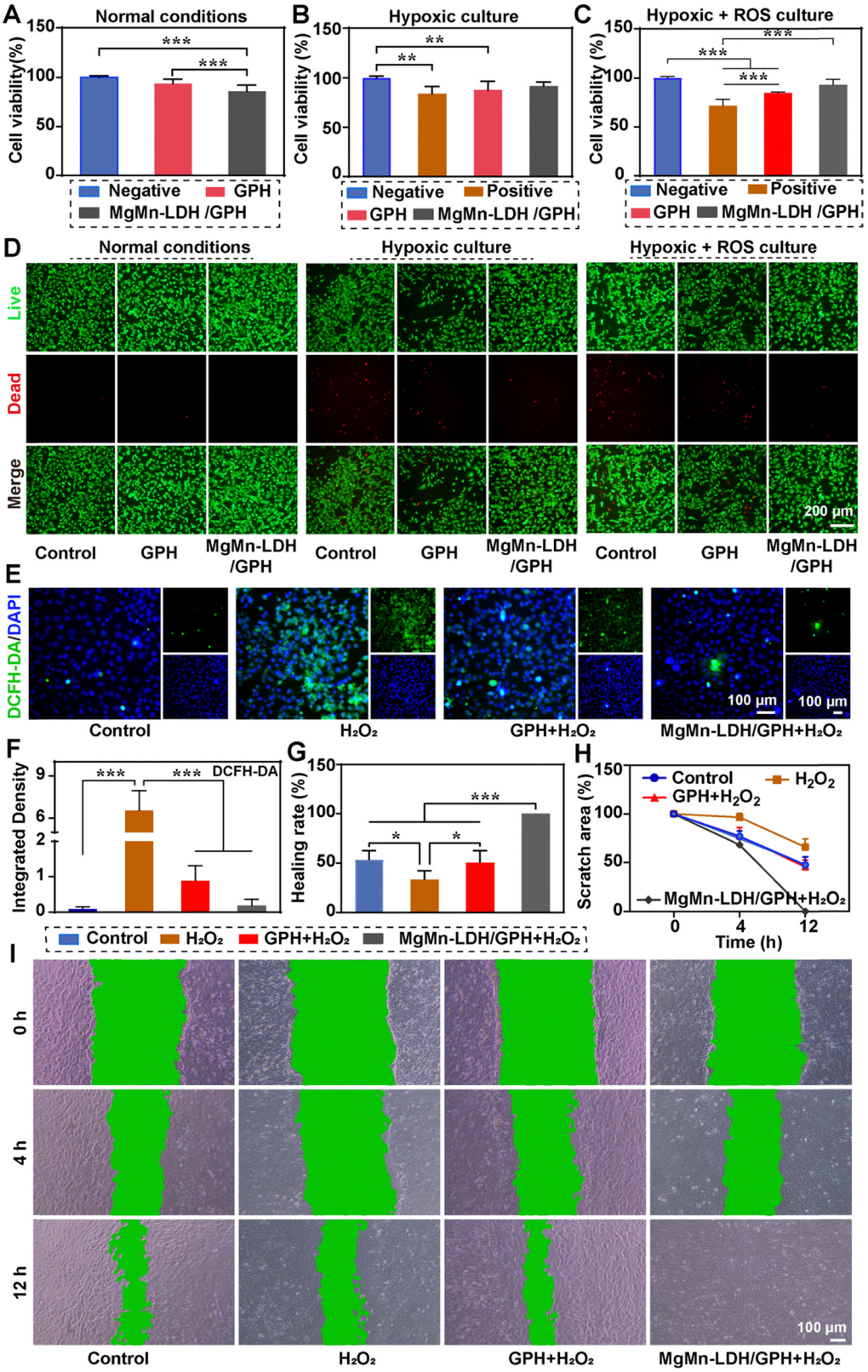

Fig. 4 Evaluation of the cytoprotective and migration-promoting effects of hydrogels. (A) Detection results of cell viability of different hydrogels under normal culture conditions; (B) detection results of cell viability of different hydrogels under hypoxic culture conditions; (C) detection results of cell viability of different hydrogels under hypoxic + H_2O_2 co-treatment conditions; (D) fluorescent images of live/dead cell staining of different hydrogels under normal culture, hypoxic culture and hypoxic + H_2O_2 co-treatment conditions; (E) fluorescent images of reactive oxygen species (ROS) in cells cultured with different hydrogels after H_2O_2 induction; (F) quantitative analysis results of ROS fluorescence intensity; (G) quantitative statistical results of cell migration rate in cells cultured with different hydrogels after H_2O_2 induction; (H) quantitative statistical results of cell scratch area in cells cultured with different hydrogels after H_2O_2 induction; (I) microscopic images of cell scratch assays in cells cultured with different hydrogels after H_2O_2 induction.

the positive group decreased to 84.0% ± 7.0%, whereas the MgMn-LDH/GPH group significantly increased to 91.7% ± 4.2%, demonstrating a remarkable hypoxic protective effect, which was mainly attributed to the oxygen-generating function of MgMn-LDH/GPH hydrogels. Under combined hypoxic + ROS stress conditions (Fig. 4C), the viability of the positive group was only 71.6% ± 6.8%, that of the GPH group was 84.5% ± 1.3%, while the MgMn-LDH/GPH group reached as high as 92.7% ± 5.9%. These results indicated that the integration of MgMn-LDH with GPH hydrogels significantly enhanced the protective capacity of the hydrogel for C17.2 cells, especially in the hyperoxidative stress and hypoxic microenvironment simulating the acute phase of SCI.[46] Live/dead cell staining further intuitively confirmed the above protective effects, as shown in Fig. 4D. Under normal conditions, all groups exhibited dense green fluorescence (viable cells) with minimal red fluorescence (dead cells). Under hypoxic conditions, the number of dead cells increased significantly, while the MgMn-LDH/GPH group showed a marked reduction in dead cells, almost restoring to the normal level with significant improvement. Under hypoxic + ROS conditions, red fluorescence dominated in the control and GPH groups, whereas green fluorescence remained predominant in the MgMn-LDH/GPH group, indicating an extremely low proportion of dead cells. Subsequently, the oxidative stress status of C17.2 cells in the ROS environment was explored using the DCFH-DA fluorescent probe. As shown in Fig. 4E, ROS-positive cells in the H_2O_2 group exhibited intense green fluorescence, indicating that C17.2 cells were in a state of oxidative stress. In contrast, green fluorescence was significantly reduced in the MgMn-LDH/GPH group, which was verified by the quantification of fluorescence intensity (Fig. 4F). This phenomenon was mainly attributed to the fact that Mn^{3+} efficiently catalyzes the decomposition of ROS into O_2 and H_2O by mimicking peroxidase-like activity, while the catechol moieties assist in free radical scavenging. This process not only alleviated oxidative stress-induced damage but also improved the hypoxic microenvironment through oxygen generation.[47] The scratch wound healing assay was performed to evaluate the effect of MgMn-LDH/GPH hydrogels on the migration of C17.2 cells. As shown in Fig. 4I, at 0 h, the scratch width was similar across all groups. In the H_2O_2-induced oxidative stress environment, the H_2O_2 group showed slow migration with a large scratch area at 12 h, while the control and GPH + H_2O_2 groups exhibited slight improvements. Notably, the scratch in the MgMn-LDH/GPH + H_2O_2 group was almost completely closed. Further quantitative analysis of the relative migration rate (Fig. 4G) and scratch area (Fig. 4H) confirmed that MgMn-LDH/GPH significantly promoted the migration of C17.2 cells towards the injured area, mimicking axon regeneration *in vivo*. Collectively, these results demonstrated that MgMn-LDH/GPH hydrogels exerted multiple synergistic effects in the *in vitro* simulated SCI microenvironment. The incorporation of MgMn-LDH enabled endogenous oxygen generation, where Mn^{3+} catalyzes oxygen production and scavenges ROS, rapidly alleviating oxidative stress and hypoxia-induced apoptosis of C17.2 cells, and played a key role in promoting the migration of C17.2 cells. Thus, this hydrogel hold great promise for achieving efficient neural tissue regeneration.

3.5. Evaluation of immunomodulatory and neural differentiation effects of MgMn-LDH@GPH hydrogels

To evaluate the regulatory effect of MgMn-LDH@GPH hydrogels on macrophage phenotypes, we established an *in vitro* inflammatory model by inducing RAW264.7 macrophages with lipopolysaccharide (LPS).[48] Immunofluorescence staining results (Fig. 5A) showed weak fluorescence for both iNOS and CD206 in the control group. In the LPS group, iNOS fluorescence was significantly enhanced, while CD206 fluorescence almost disappeared, indicating macrophage polarization toward the M1 phenotype. In the MgMn-LDH@GPH group, iNOS fluorescence was drastically reduced, and CD206 fluorescence was restored to a high level, demonstrating that the hydrogel effectively reversed LPS-induced M1 polarization. Quantitative analysis of fluorescence intensity (Fig. 5B) further confirmed that the iNOS fluorescence intensity in the LPS group was 11.6-fold higher than that in the control group. In the MgMn-LDH@GPH group, CD206 expression increased by 8.6-fold, while iNOS expression decreased to 0.3-fold of the control group. These results indicated that the incorporation of MgMn-LDH significantly enhancesd the immunomodulatory capacity of the hydrogel.[49] The immunomodulatory effect of MgMn-LDH@GPH hydrogels was further evaluated by flow cytometry (Fig. 5D). In the LPS group, the proportion of $CD86^+$ cells was as high as 16.86%, while the proportion of $CD206^+$ cells was only 0.32%. In contrast, in the MgMn-LDH/GPH + LPS group, the proportion of $CD86^+$ cells further decreased to 1.85%, and $CD206^+$ cells increased to 13.09%. Quantitative analysis of the CD86/CD206 ratio (Fig. 5C) showed that the ratio in the LPS group was 26.8-fold higher than that in the control group, while it was only 0.08-fold in the MgMn-LDH/GPH + LPS group. qPCR analysis (Fig. 5E and Fig. S3) revealed that the relative expression levels of M1 pro-inflammatory genes Nos2, Tnfα, iNOS and CD86 in the LPS group were significantly higher than those in the control group, but were markedly reduced in the MgMn-LDH/GPH + LPS group. In contrast, the relative expression levels of classical M2 markers Arg1, Il10 and CD206 in the MgMn-LDH/GPH + LPS group were significantly higher than those in the LPS and GPH + LPS groups, restoring to the levels of the control group. These results were highly consistent with the aforementioned immunofluorescence and flow cytometry data. To further investigate the effect of the hydrogel on neural differentiation, we used C17.2 cells to simulate the neural stem cell differentiation process. Cytoskeleton staining results (Fig. 5H) showed that on days 3 and 5, the control group had short cell neurites, the H_2O_2 group had almost no neurites, and the GPH + H_2O_2 group showed slight neurite recovery. Notably, the MgMn-LDH/GPH + H_2O_2 group exhibited significantly elongated neurites forming a dense network. This was attributed to the release of Mg^{2+} from MgMn-LDH/GPH. As an important neuroprotective factor, Mg^{2+} blocked the excessive activation of NMDA receptors, promoted the phosphorylated activation of the PI3K/Akt

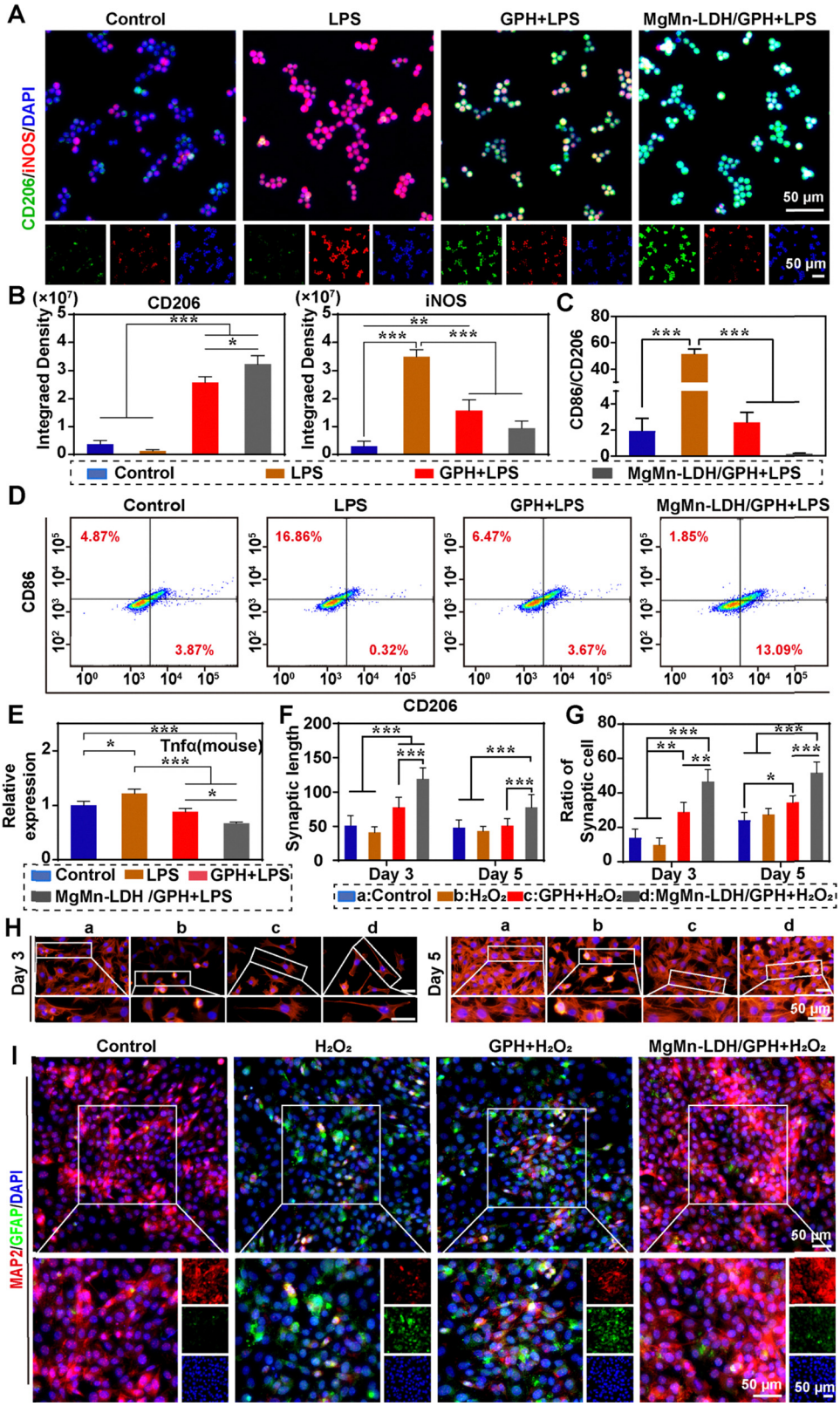

Fig. 5 Regulatory effects of hydrogels on macrophage polarization and neural cell repair under inflammatory stimulation and oxidative stress. (A) Immunofluorescence staining images of CD206, iNOS and DAPI in RAW264.7 cells cultured with different hydrogels; (B) quantitative statistical analysis results of the fluorescence intensity of CD206 and iNOS; (C) CD86/CD206 ratio of different macrophage phenotypes detected by flow cytometry in RAW264.7 cells cultured with different hydrogels; (D) flow cytometry (FACS) dot plots of CD86 and CD206 in RAW264.7 cells cultured with different hydrogels; (E) detection of Tnfα mRNA expression levels in RAW264.7 cells by qPCR; (F) quantitative statistics of neurite length in cells cultured with different hydrogels under H_2O_2-induced oxidative stress; (G) statistical analysis of the proportion of neurite-bearing cells in cells cultured with different hydrogels under H_2O_2-induced oxidative stress; (H) immunofluorescence images showing changes in neurite morphology of cells at 3 and 5 days of culture with different hydrogels; (I) immunofluorescence staining images of GFAP, MAP2 and DAPI in neuronal cells under H_2O_2-induced oxidative stress.

signaling pathway, enhances neuronal survival, inhibited neuronal apoptosis, and facilitates axonal outgrowth.[50] Quantitative analysis of neurite length (Fig. 5F) showed that on day 5, the neurite length in the MgMn-LDH/GPH + H_2O_2 group was 1.6-fold that of the control group. Subsequent quantitative analysis of the proportion of neurite-bearing cells (Fig. 5G) showed that it increased to 51.3% on day 5, which was 2.11-fold higher than that in the control group. To verify the neuronal differentiation efficiency of C17.2 cells, double staining for MAP-2 and GFAP was performed (Fig. 5I). The control group showed strong MAP-2 fluorescence and weak GFAP fluorescence. Compared with the control group, the H_2O_2 group exhibited significantly reduced MAP-2 fluorescence, indicating impaired neuronal differentiation of C17.2 cells. In the MgMn-LDH/GPH + H_2O_2 group, MAP-2 fluorescence was significantly enhanced, while GFAP remained at a low level, suggesting that C17.2 cells preferentially differentiated into neurons. This was because Mg^{2+} could modulate the activation of MAPK, thereby promoting the proliferation, differentiation and axonal guidance of neural stem/progenitor cells.[51] Additionally, quantitative analysis of MAP-2 and GFAP fluorescence intensity (Fig. S4) showed that MAP-2 expression in the H_2O_2 group was significantly lower than that in the control group, whereas it was significantly increased in the MgMn-LDH/GPH + H_2O_2 group, even exceeding the control group level. In contrast, GFAP expression was significantly inhibited in the MgMn-LDH/GPH + H_2O_2 group, restoring to near-normal levels, indicating that the hydrogel effectively blocked the oxidative stress-induced gliosis tendency.[52] Subsequently, we investigated the regulatory effects of MgMn-LDH/GPH on the PI3K/Akt and MAPK signaling pathways *via* qPCR, with the results presented in Fig. S5. The expression levels of downstream factors of the PI3K/Akt and MAPK signaling pathways were significantly decreased under H_2O_2 stimulation, indicating that these two pathways were markedly inhibited. After treatment with MgMn-LDH/GPH, the expression levels of the aforementioned downstream factors were significantly upregulated, which demonstrated that the inhibition of the PI3K/Akt and MAPK signaling pathways was alleviated, and the adverse effects of ROS on these two signaling pathways were effectively abrogated. Collectively, these results confirmed the multiple immunomodulatory and neural differentiation-promoting effects of MgMn-LDH/GPH hydrogels. In the LPS-induced inflammatory model, MgMn-LDH/GPH hydrogels reversed M1 macrophage polarization to M2, reduced the expression of pro-inflammatory cytokine, and increased the expression of anti-inflammatory cytokine levels. Furthermore, in an oxidative stress environment, the hydrogel promoted neurite outgrowth of C17.2 cells and differentiation into MAP-2-positive neurons. These findings provide a cellular basis for the axonal regeneration and functional recovery observed in *in vivo* SCI models, highlighting the clinical potential of this hydrogel in reprogramming the spinal cord injury microenvironment.

3.6. MgMn-LDH/GPH hydrogel promotes the recovery of motor function in rats after spinal cord injury

Previous studies have indicated that spinal cord injury can lead to severe neural network disruption and loss of neurological function. However, the neural structure and pathophysiological characteristics of the injured spinal cord were closely associated with motor function in animals.[53] Injectable hydrogels were considered excellent carriers for promoting neural tissue regeneration and could be utilized for spinal cord injury repair when loaded with active components. To evaluate the *in vivo* therapeutic efficacy of MgMn-LDH/GPH hydrogel, we employed a rat model of complete T10 spinal cord transection. The animal experimental scheme was illustrated in Fig. 6A. Following the successful establishment of the spinal cord injury model, MgMn-LDH/GPH hydrogel was immediately injected into the lesion cavity to fill the void (Fig. 6B). The therapeutic efficacy of MgMn-LDH/GPH hydrogel was then evaluated through behavioral and histological analyses. The Basso, Beattie, and Bresnahan (BBB) scoring systemwas used to hindlimb motor function from days 0 to 42 post-surgery. As shown in Fig. 6C, all rats initially presented a BBB score of 0, indicative of complete hindlimb paralysis. By day 42, the SCI group achieved a score of only 2.3 $\pm$ 0.6, demonstrating limited spontaneous recovery. In contrast, the MgMn-LDH/GPH hydrogel group exhibited the most significant functional recovery, attaining a final BBB score of 11.3 $\pm$ 0.6, which was significantly higher than that in the GPH hydrogel-alone group (9.0 $\pm$ 1.7). The footprint analysis results were shown in Fig. 6D and E. Rats in the SCI group exhibited severe dragging of their hindlimbs. In contrast, the MgMn-LDH/GPH hydrogel group displayed clear hindlimb footprints and achieved stable stepping with coordinated forelimb-hindlimb movement, approximating a normal gait. These findings indicated that MgMn-LDH/GPH hydrogel significantly improved motor function. The pivotal factor underlying this marked functional recovery was the sustained and controlled release of MgMn-LDH components, which cleared ROS in the injured spinal cord microenvironment and promoted neural regeneration.[54] At 14 and 42 days post-surgery, HE staining was performed to assess the recovery of the spinal cord cavity around the injury site (Fig. 6F). In the SCI group, large cavities were observed at the lesion epicenter on both day 14 and 42, with minimal nascent tissue infiltration. The GPH group exhibited some tissue ingrowth but still displayed noticeable cavities and relatively loose cellular infiltration at the injury site. In contrast, the MgMn-LDH/GPH hydrogel group showed continuous nascent tissue bridging as early as day 14. By day 42, the lesion area was almost completely filled with dense extracellular matrix and new tissue, resulting in the near disappearance of the cavity. This superior repair was likely attributable to the MgMn-LDH/GPH hydrogel, which improved the pathological microenvironment, facilitated endogenous cell migration, and bridinated the lesion gap by serving as a supportive scaffold. A common and severe complication of spinal cord injury was bladder dysfunction, which consequently lead to significant issues such as urinary tract infections and incontinence.[55] Masson staining of bladder tissue (Fig. 6G) revealed an improved pathological environment in the MgMn-LDH/GPH hydrogel group compared to the SCI group. This was evidenced by significantly thickened bladder walls and reduced tissue vacuolization. Furthermore, quantitative

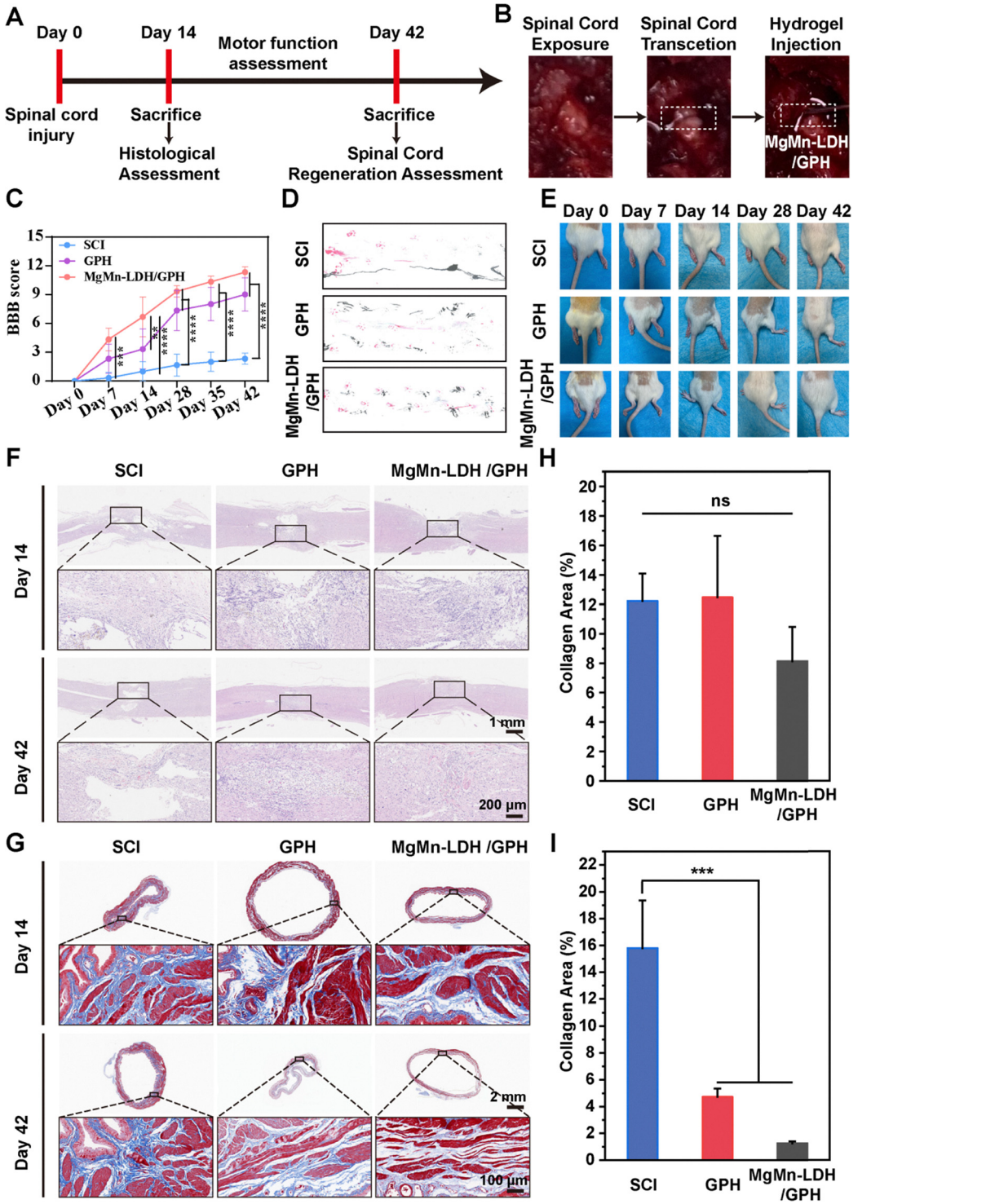

Fig. 6 MgMn-LDH@GPH hydrogel promotes motor function recovery after SC in rats. (A) Schematic diagram of the animal experimental protocol; (B) photographs of the surgical procedure; (C) BBB motor function score curves from 0 to 42 days postoperatively; (D) footprint analyses of each group on day 42; (E) photographs of the hind limbs of rats in each group from 0 to 42 days postoperatively; (G) HE staining of the spinal cord on days 14 and 42; (H) Masson staining of bladder tissues on days 14 and 42; (I) quantitative statistics of collagen in bladder tissues on day 14; (J) quantitative statistics of collagen in bladder tissues on day 42.

analysis of the collagen scar area (Fig. 6H and I) showed no significant difference at day 14. However, by day 42, the collagen deposition area in the MgMn-LDH/GPH hydrogel group was substantially reduced to 1.3% ± 0.2%, which was significantly lower than that in the SCI group (15.8% ± 3.6%), representing an inhibition of collagen scarring by over 92.8%. These findings demonstrated that the MgMn-LDH/GPH hydrogel protected the urinary system effectively *via* its ROS/pH dual-

responsive release of active components. It achieved this by preventing the formation of dense collagen scars, thereby creating a regeneration-friendly microenvironment conducive to long-distance growth of neurons and axons, which further corroborated its positive role in spinal cord repair.

3.7. Evaluation of inflammatory regulation and apoptosis inhibition of MgMn-LDH/GPH hydrogels for SCI repair

To evaluate the repair efficacy of MgMn-LDH/GPH hydrogels in a rat T10 complete transection SCI model, spinal cord tissues were harvested on day 14 and day 42 post-surgery for DCFH-DA, TUNEL, and CD68 immunofluorescence staining analyses. DCFH-DA staining results (Fig. 7A) showed intense and dense distribution of red fluorescence in the injured area of the SCI group on day 14, indicating persistent oxidative stress. The GPH group exhibited slightly reduced fluorescence, but it remained significant. In contrast, the fluorescence in the MgMn-LDH/GPH group almost disappeared, with the injured area approaching the level of normal spinal cord tissue. Quantitative analysis of fluorescence intensity (Fig. 7B) further confirmed that the fluorescence intensity in the MgMn-LDH/GPH group was only 6.0% of that in the SCI group, representing a 94.0% reduction. These results demonstrated that the hydrogel efficiently catalyzes the decomposition of ROS into O_2 *via* Mn^{3+} *in vivo*, continuously scavenged excessive ROS in the injured area, and alleviated the oxidative microenvironment.[56] TUNEL staining results (Fig. 7C) revealed massive accumulation of apoptotic cells in the injured area of the SCI group on day 14,

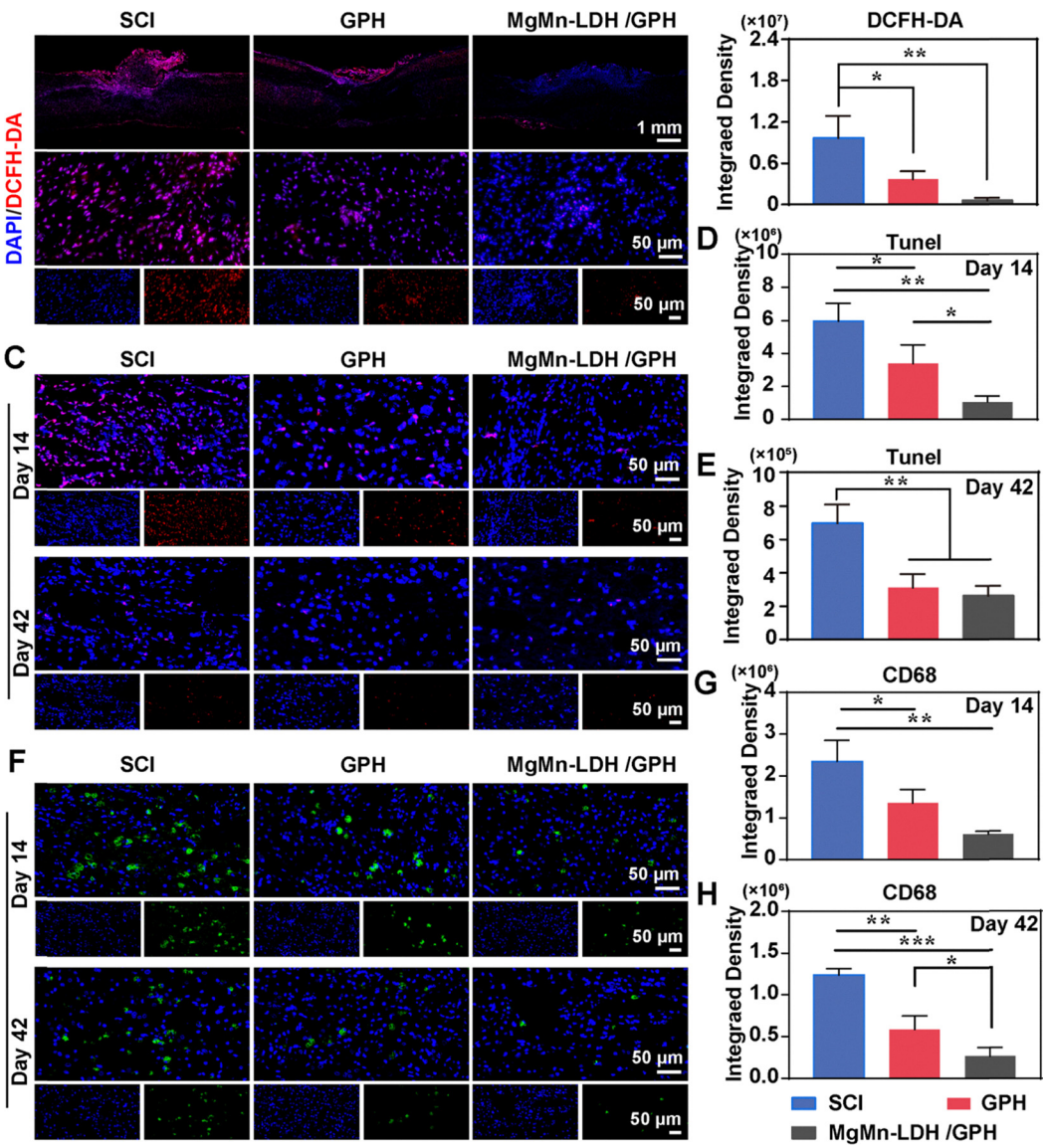

Fig. 7 Regulatory effects of hydrogels on ROS levels, cell apoptosis, and macrophage infiltration during SCI repair. (A) DCFH-DA staining to assess ROS levels at the spinal cord injury site on day 14; (B) quantitative analysis of ROS fluorescence intensity; (C) TUNEL staining to detect apoptotic cells on day 14 and day 42; (D and E) quantitative analysis of TUNEL fluorescence intensity; (F) CD68 immunofluorescence staining to observe macrophage infiltration; (G–H) quantitative statistics of CD68 expression levels.

whereas the apoptotic signal was significantly attenuated in the MgMn-LDH/GPH group. By day 42, a small amount of apoptotic signal was still detectable in the SCI and GPH groups, but almost no TUNEL-positive apoptotic cells were observed in the MgMn-LDH/GPH group. Quantitative statistical results (Fig. 7D and E) showed that the TUNEL fluorescence intensity in the MgMn-LDH/GPH group was 17.5% of that in the SCI group on day 14, and further decreased to 37.7% on day 42. This confirmed that the hydrogel significantly protected cells and neurons from apoptosis through ROS scavenging. CD68 staining results (Fig. 7F) showed highly dense green fluorescence in the injured area of the SCI group on day 14, indicating severe inflammatory infiltration in this region. The number of CD68-positive cells was significantly reduced in the MgMn-LDH/GPH group, suggesting alleviation of the inflammatory microenvironment. By day 42, mild and persistent inflammatory signals

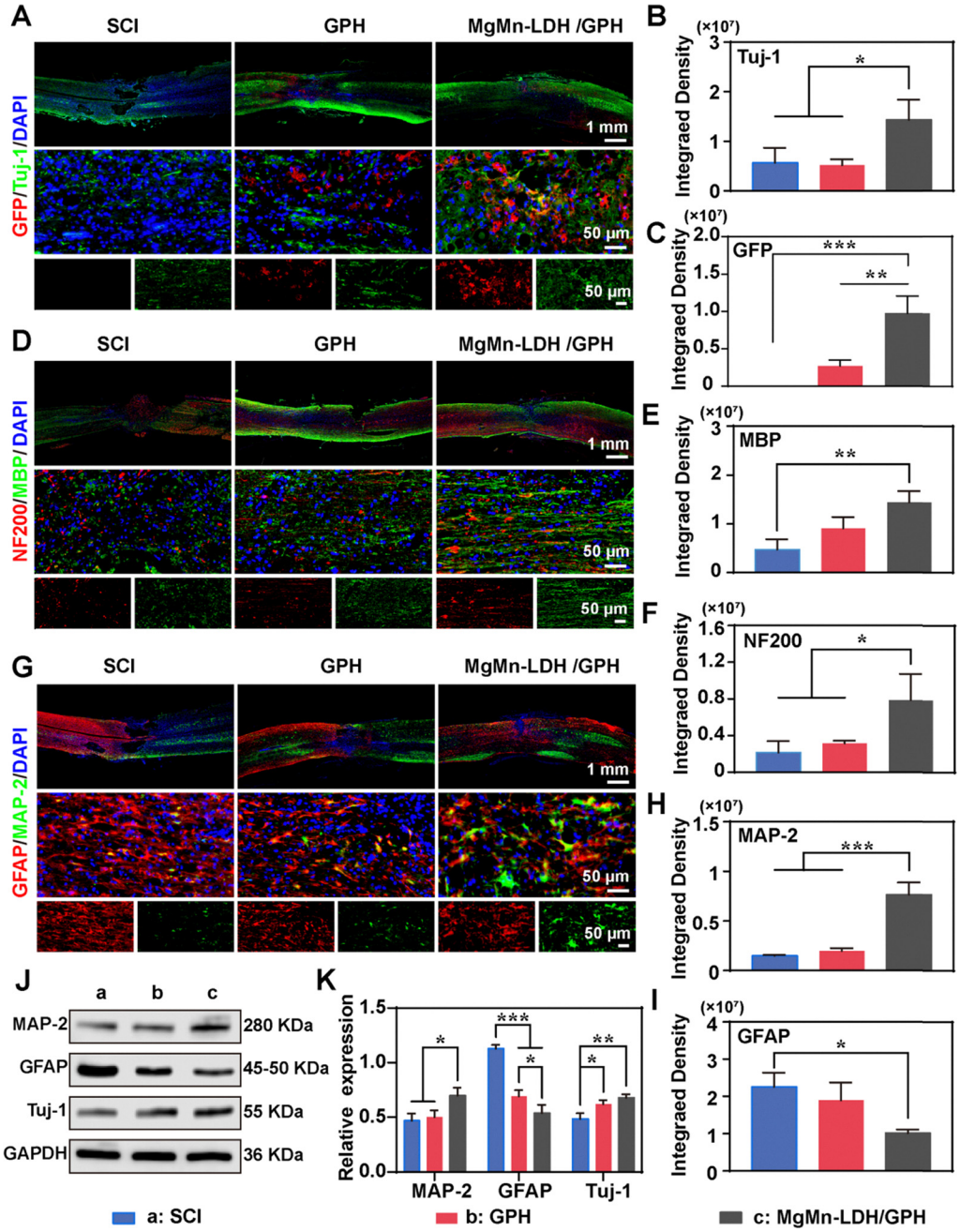

Fig. 8 Effects of hydrogels on neuroregeneration, myelination, and glial scar regulation during SCI repair. (A) Immunofluorescence staining images of Tuj-1, GFP, and DAPI at 42 days post-treatment; quantitative analysis of Tuj-1 (B) and GFP (C) fluorescence intensity; (D) immunofluorescence staining images of MBP and NF200 at 42 days post-treatment; quantitative analysis of MBP (E) and NF200 (F) fluorescence intensity; (G) immunofluorescence staining images of MAP-2 and GFAP at 42 days post-treatment; quantitative results of MAP-2 (H) and GFAP (I) fluorescence intensity; (J) western blot analysis of MAP-2, GFAP, and Tuj-1 protein expression levels in spinal cord tissues at 42 days post-treatment, with GAPDH as the loading control; (K) quantitative gray value analysis results of western blot bands.

were still observed in the SCI and GPH groups, while no green fluorescence was detected in the MgMn-LDH/GPH group, demonstrating effective regulation of the inflammatory environment. Quantitative analysis (Fig. 7G and H) indicated that the CD68 fluorescence intensity in the MgMn-LDH/GPH group was 25.9% of that in the SCI group on day 14, and decreased to 21.4% on day 42. Collectively, these results confirmed the multifunctional synergistic therapeutic effects of MgMn-LDH/GPH hydrogels in the SCI model. The MgMn-LDH/GPH hydrogel catalyzed oxygen generation and scavenges ROS, rapidly reducing DCFH-DA-positive signals, while blocking the TUNEL-positive apoptotic cascade. Additionally, it induces M2 macrophage polarization and reduces $CD68^+$ inflammatory cell recruitment, achieving more comprehensive microenvironment reprogramming in the complete transection SCI model.

3.8. Evaluation of neuroregenerative efficacy of MgMn-LDH/GPH hydrogel for SCI repair

To further verify the neuroregenerative efficacy of MgMn-LDH/GPH hydrogels in a rat T10 complete transection SCI model, GFP/Tuj-1, NF200/MBP, and GFAP/MAP-2 double immunofluorescence staining as well as western blot analysis were performed on day 42 post-surgery. GFP/Tuj-1 double staining results (Fig. 8A) showed extremely weak red fluorescence of Tuj-1 in the injured area of the SCI group, indicating a small number of newborn neurons that were only visible at the edge, with obvious discontinuity in the injured region. The GPH group exhibited slightly increased but unevenly distributed fluorescence. Notably, the injured area in the MgMn-LDH/GPH group was completely restored, with dense Tuj-1-positive cells observed in the injury center, suggesting the differentiation of neural cells into neurons.[57] Quantitative analysis of fluorescence intensity (Fig. 8B and C) revealed that the GFP fluorescence intensity in the MgMn-LDH/GPH group was significantly higher than that in the SCI group, confirming the complete recovery of the spinal cord injury site. Additionally, the Tuj-1 fluorescence intensity in the MgMn-LDH/GPH group was 2.5-fold that of the SCI group, indicating a significant increase in the density of newborn neurons. NF200/MBP double immunofluorescence staining results (Fig. 8D) showed extremely weak fluorescence of NF200 and MBP in the injured area of the SCI group, indicating minimal axonal and myelin regeneration with almost no continuous fibers. The GPH group showed a small number of short axons but incomplete myelin sheaths. In contrast, the MgMn-LDH/GPH group displayed long-distance axonal bundles wrapped by uniform MBP, forming typical regenerated nerve bundles. Quantitative analysis of fluorescence intensity (Fig. 8E and F) demonstrated that the NF200 fluorescence intensity in the MgMn-LDH/GPH group was 3.7-fold that of the SCI group, and the MBP fluorescence intensity was 3.0-fold higher, indicating that MgMn-LDH/GPH hydrogels accelerated nerve bundle regeneration.[58] GFAP/MAP-2 double immunofluorescence staining results (Fig. 8G) showed strong and dense red fluorescence of GFAP and weak green fluorescence of MAP-2 in the injured area of the SCI group, indicating severe glial scarring and a small number of mature neurons. The GPH group exhibited slightly reduced GFAP fluorescence but still low MAP-2 expression. In the MgMn-LDH/GPH group, GFAP fluorescence was significantly attenuated, while MAP-2 fluorescence was enhanced, demonstrating the inhibition of glial scarring and promotion of mature neuron formation.[59] Quantitative statistics (Fig. 8H and I) confirmed that the MgMn-LDH/GPH group had the weakest GFAP fluorescence intensity and the strongest MAP-2 fluorescence intensity, which was 5.2-fold that of the SCI group. Western blot results (Fig. 8J) showed weak bands of MAP-2 and Tuj-1 but strong GFAP bands in the spinal cord tissues of the SCI group. In contrast, the MgMn-LDH/GPH group exhibited significantly enhanced MAP-2/Tuj-1 expression and drastically reduced GFAP levels. Quantitative statistical results (Fig. 8K) verified that the relative expression levels of MAP-2, GFAP, and Tuj-1 in the MgMn-LDH/GPH group were 1.5-fold, 0.5-fold, and 1.4-fold those of the SCI group, respectively. Collectively, these results confirmed the multiple neuroregenerative mechanisms of MgMn-LDH@GPH hydrogels. The hydrogel upregulated neuronal markers such as Tuj-1 and MAP-2 to promote the differentiation of transplanted cells into mature neurons, while inhibiting GFAP expression to block glial scar formation and synergistically facilitating long-distance axonal regeneration and myelination. It had achieved superior neural repair effects in the complete transection spinal cord injury (SCI) model, highlighting its great potential in clinical SCI treatment.

4. Conclusion

In summary, screening of bioactive metal ions revealed that Mn^{3+} and Mg^{2+} significantly mitigate oxidative stress and inflammation by scavenging reactive oxygen species (ROS) and promoting anti-inflammatory M2 macrophage polarization. The synergistic effects of Mn^{3+} and Mg^{2+} markedly improved the spinal cord injury (SCI) microenvironment. Magnesium-manganese layered double hydroxides (MgMn-LDHs) were designed to neutralize acidic conditions and deliver Mn^{3+} and Mg^{2+}, enhancing their roles in neural repair and immune modulation. Molecular analyses, including immunofluorescence staining and western blot, confirmed that MgMn-LDHs significantly accelerated neural differentiation, promoting axonal growth, myelination, and vascular regeneration. Notably, MgMn-LDHs induced the release of neurotrophic factors, facilitating PC12 cell proliferation and neurite outgrowth. Furthermore, integration of MgMn-LDHs into ROS- and pH-responsive GelMA-PBA/HA-DA hydrogels demonstrated superior tissue regeneration, inflammation suppression, and locomotor recovery in mouse SCI models. These findings provided novel insights into bioactive nanoplatforms for SCI repair, highlighting the therapeutic potential of Mn^{3+}- and Mg^{2+}-mediated microenvironment modulation in treating central nervous system injuries.

5. Future directions

This study designed a pH/ROS-responsive hydrogel loaded with MgMn-LDH for the microenvironment of spinal cord injury

(SCI) repair. Systematic *in vitro* and *in vivo* studies verified the therapeutic efficacy of MgMn-LDH/GPH in SCI repair, and the results demonstrated that it exerted a significant promotional effect on SCI repair. However, this study still warrants further in-depth investigation in the following aspects. First, the interlayer spacing, metal ion ratio, or surface modification of MgMn-LDH can be further regulated to achieve hierarchical responses to different concentrations and types of ROS. Alternatively, the introduction of other bioactive ions and nanoenzymes can be explored to construct a multi-enzyme mimetic system, thereby further enhancing the ROS scavenging efficiency and O_2 release capacity. Second, single-cell RNA sequencing or transcriptomics sequencing can be performed to further analyze the transcriptomic changes after hydrogel treatment, revealing more refined molecular interaction networks. Meanwhile, specific pathway inhibitors can be used to verify the causal regulatory effects of Mg^{2+}/Mn^{3+} on key signaling pathways such as PI3K/Akt, MAPK, and Nrf2. Finally, this hydrogel system can be extended to other neural injury models, combined with other therapeutic strategies to evaluate the synergistic enhancement potential, and promote the feasibility assessment of bench-to-clinic translation.

Author contributions

Lian Ren: investigation, conceptualization and data curation. Xiaobin Zhou: formal analysis and roles/writing – original draft. Longbao Feng: investigation. Guodong Sun: funding acquisition and supervision.

Conflicts of interest

The authors declare no competing financial interest.

Data availability

The data supporting this study are not openly accessible owing to the protection of research participant privacy.

Supplementary information (ESI) available. See DOI: https://doi.org/10.1039/d6ma00108d.

Acknowledgements

This study was financially supported by the National Nature Science Foundation of China (82171372), Natural Science Foundation of Guangdong Province (2023A1515010521), Guangdong Provincial Key Laboratory of Laboratory of Spine and Spinal Cord Reconstruction (2023B121203001), The Science and Technology Program of Heyuan, China (Heyuan Technology platform NO. 2022003, Heyuan Technology platform NO. 008), The Science and Technology Project of Heyuan, China (Social Development and Rural Science No. 2023004), Natural Science Foundation of Hunan Province (2026JJ80419).

References

1 J. Yang, K. Yang, W. Man, J. Zheng, Z. Cao, C.-Y. Yang, K. Kim, S. Yang, Z. Hou, G. Wang and X. Wang, 3D bioprinted living nerve-like fibers refine the ecological niche for long-distance spinal cord injury regeneration, *Bioact. Mater.*, 2023, **25**, 160–175.

2 J. Wu, J. Tang, L. Zhang, W. Wang, Z. Li, L. Zhou, X. Jiang, Y. Huang, Q. Guo, W. Wang, Z. Ding, F. Cai, K. Xi, Y. Gu and L. Chen, Biomimetic ''Trojan Horse'' Fibers Modulate Innate Immunity Cascades for Nerve Regeneration, *ACS Nano*, 2025, **19**(1), 781–802.

3 Q. Zheng, D. Wang, R. Lin and W. Xu, Pyroptosis, ferroptosis, and autophagy in spinal cord injury: regulatory mechanisms and therapeutic targets, *Neural Regener. Res.*, 2025, **20**(10), 2787–2806.

4 J. Lv, S. Ma and D. Shan, Precision Nanotherapy for Spinal Cord Injury: Modulating SLC16A3 With Methylprednisolone-Loaded Nanoparticles, *Neurospine*, 2025, **22**(2), 478–499.

5 X. Zhang, W. Zhang, H. Sun and H. Wang, The effects of exosomes originating from different cell sources on the differentiation of bone marrow mesenchymal stem cells into Schwann cells, *J. Nanobiotechnol.*, 2024, **22**(1), 220.

6 B. Dai, Z. Fan, R. Chen, X. Weng and R. Fang, Mechanistic Study of Jaceosidin in Regulating Secondary Inflammation After Spinal Cord Injury in Mouse by Inhibiting PKM2 Activity, *NeuroMol. Med.*, 2025, **27**(1), 57.

7 C.-w Ma, Z.-q Wang, R. Ran, H.-y Liao, J.-y Lyu, Y. Ren, Z.-y Lei and H.-h Zhang, TGF-β signaling pathway in spinal cord injury: Mechanisms and therapeutic potential, *J. Neurosci. Res.*, 2024, **102**(1), e25255.

8 J. Zheng, T. Chen, K. Wang, C. Peng, M. Zhao, Q. Xie, B. Li, H. Lin, Z. Zhao, Z. Ji, B. Z. Tang and Y. Liao, Engineered Multifunctional Zinc–Organic Framework-Based Aggregation-Induced Emission Nanozyme for Accelerating Spinal Cord Injury Recovery, *ACS Nano*, 2024, **18**(3), 2355–2369.

9 Y. You, J. Jiang, G. Zheng, Z. Chen, Y.-X. Zhu, H. Ma, H. Lin, X. Guo and J. Shi, In Situ Piezoelectric-Catalytic Anti-Inflammation Promotes the Rehabilitation of Acute Spinal Cord Injury in Synergy, *Adv. Mater.*, 2024, **36**(18), 2311429.

10 H. Zhou, Z. Li, S. Jing, B. Wang, Z. Ye, W. Xiong, Y. Liu, Y. Liu, C. Xu, T. Kumeria, Y. He and Q. Ye, Repair spinal cord injury with a versatile anti-oxidant and neural regenerative nanoplatform, *J. Nanobiotechnol.*, 2024, **22**(1), 351.

11 X. Wang, Z. Zhou, Y. Zhang, J. Liu, T. Qin, W. Zhou, Q. Li, X. Wu, K. Xue, H. Cao, Y. Su, S. Zhao, C. Lu, T. Jiang, G. yin and J. Chen, Exosome-shuttled miR-5121 from A2 astrocytes promotes BSCB repair after traumatic SCI by activating autophagy in vascular endothelial cells, *J. Nanobiotechnol.*, 2025, **23**(1), 291.

12 S. Li, S. Yuan, S. Yang, C. Zhou, Y. Zhong, Z. Huang, C. Meng, L. Pei, Y. Xie, X. Chen, H. Wu, Y. Guo, H. Long and T. Wang, Apelin-13/APJ promotes neural stem cells to repair ischemic stroke, *Tissue Cell*, 2025, **95**, 102872.

13 P. Zhu, L. Ge, T. Luo, M. Qin, Y. Xu, R. Hua, S. Lu, M. Jin, N. Chen, J. He, Q. Liu, Z. Ruan, L. Yang and H. Zhang, Multifunctional MXene-Based Hydrogel Remodels Regenerative Microenvironment and Facilitates Neurogenesis of Endogenous Neural Stem Cells for Spinal Cord Injury Recovery, *ACS Appl. Nano Mater.*, 2025, **8**(13), 6361–6379.

14 B. Y. A. Hollingworth, P. N. Pallier, S. I. Jenkins and R. Chen, Hypoxic Neuroinflammation in the Pathogenesis of Multiple Sclerosis, *Brain Sci.*, 2025, 248.

15 S. Xian, S. Yang, Z. Liao, Y. Jiang, Y. Leng, J. Ning, H. Gao, Z. Xiao and X. Shuai, Engineering Mesenchymal Stem Cells with Antioxidant Catalase-Loaded Metal–Organic Frameworks for Targeted Spinal Cord Injury Therapy, *Adv. Funct. Mater.*, 2025, **35**(48), 2500726.

16 Y.-Y. Wu, Y.-M. Gao, T. Feng, J.-S. Rao and C. Zhao, Enhancing Functional Recovery After Spinal Cord Injury Through Neuroplasticity: A Comprehensive Review, *Int. J. Mol. Sci.*, 2025, 6596.

17 S. Zhu, S. Diao, X. Liu, Z. Zhang, F. Liu, W. Chen, X. Lu, H. Luo, X. Cheng, Q. Liao, Z. Li and J. Chen, Biomaterial-based strategies: a new era in spinal cord injury treatment, *Neural Regener. Res.*, 2025, **20**(12), 3476–3500.

18 R. V. Niella, J. M. Corrêa, C. S. Marques, Á. J. Silva, L. C. Santos, I. S. Oliveira, G. DeFreitas-Silva, J. S. Rebouças, J. F. Silva and M. S. de Lavor, Manganese Porphyrin Treatment Improves Redox Status Caused by Acute Compressive Spinal Cord Trauma, *Antioxidants*, 2025, 587.

19 C. Jiang, M. Sun, Y. Wang, C. Dong, Y. Yu, G. Wang, Y. Lu and Z. Chen, Coordination Engineering in Fe-Mn Dual-Atom Nanozyme: Yielding ROS Storm to Efficiently Promote Wound Healing, *Adv. Funct. Mater.*, 2025, **35**(29), 2424599.

20 H. M. Iao, C.-Y. Chen, Y.-H. Lin, W.-C. Pan, C.-Y. Liang, H.-C. Liu, L.-J. Ching, P.-Y. Weng, M.-R. Chiang, R.-S. Hsu, T.-C. Chou, I. C. Lee, L.-D. Liao, L.-A. Chu, S.-H. Chiou and S.-H. Hu, Wireless In Situ Catalytic Electron Signaling-Mediated Transcriptomic Reprogramming for Neuron Regeneration via Adaptable Antennas, *Adv. Sci.*, 2025, **12**(28), 2504786.

21 J. Liu, Z. Yao, Z. Hu, X. Zhang, B. Gong, Y. Dai, H. Weng, L. Xiao, B. Zhang, T. Li, K. Shi, P. Xie, F. Tian, L. Rong, J. Xue and L. He, Spatiotemporal Delivery of Required Facilitators for Microenvironment Remodeling Propels Neural Regeneration after Spinal Cord Injury, *Adv. Mater.*, 2025, e03479.

22 X. Liu, B. Ma, S. Hu, D. Li, C. Pan, Z. Xu, H. Chen, Y. Wang and H. Wang, Phase-adapted metal ion supply for spinal cord repair with a Mg–Zn incorporated chimeric microsphere, *Biomaterials*, 2025, **320**, 123253.

23 H. Kim, T. Kim, K. A. Rahaman, J. Kwon, J.-Y. Lee, S. Cho, S. Chung, H.-S. Han and Y.-C. Kim, Synergistic Effects of Magnesium and Zinc Ions on Neural Stem Cell Proliferation and Differentiation, *JOM*, 2025, **77**(6), 4402–4413.

24 F. Zhang, X. Pan, K. Zhang, S. Liu, D. Yu, J. Su, T. Zhu and S. Chen, Enhancing spinal cord injury repair through PTCH1-mediated neural progenitor cell differentiation induced by ion elemental-optimized layered double hydroxides, *Mater. Today Bio*, 2025, **32**, 101918.

25 X. Yang, S. Peng, X. Chen, W. Zhang, H. Deng, L. Zhou, Y. Yan and Q. Zhang, Multi-metallic layered double hydroxides functionalized degradable bone cement: Modulation of degradation, sustained ion release, antimicrobial, and osteogenic properties, *Appl. Clay Sci.*, 2025, **265**, 107652.

26 Z. Wang, C. Gu, Y. Tang, X. Su, D. Xia, Q. Zhou, Z.-C. Xiong, Y.-J. Zhu and X. Chen, Bioactive Multifunctional Hydrogel Scaffolds Remodel the Inflammatory Microenvironment and Osteogenic-Osteoclastic Homeostasis to Advance Osteoporotic Bone Defect Repair, *ACS Nano*, 2025, **19**(50), 42538–42555.

27 M. Zhang, C. Xiang, X. Zhen, W. Luo, X. He, F. Guo, R. Niu, W. Liu and R. Gu, Natural polymer based drug-loaded hydrogel platform for comprehensive care of acute spinal cord injury, *Mater. Today Bio*, 2025, **31**, 101464.

28 C. Correia, D. Peixoto, D. Soares da Costa, R. L. Reis, I. Pashkuleva and N. M. Alves, Development and in vitro assessment of injectable, adhesive, and self-healing chitosan-based hydrogels for treatment of spinal cord injury, *Biomater. Adv.*, 2025, **167**, 214090.

29 Y. Zhu, L. Wang, Y. Li, Z. Huang, S. Luo, Y. He, H. Han, F. Raza, J. Wu and L. Ge, Injectable pH and redox dual responsive hydrogels based on self-assembled peptides for anti-tumor drug delivery, *Biomater. Sci.*, 2020, **8**(19), 5415–5426.

30 W. Yang, J. Chen, Z. Zhao, M. Wu, L. Gong, Y. Sun, C. Huang, B. Yan and H. Zeng, Recent advances in fabricating injectable hydrogels via tunable molecular interactions for bio-applications, *J. Mater. Chem. B*, 2024, **12**(2), 332–349.

31 Y. Gao, Z. Li, J. Huang, M. Zhao and J. Wu, In situ formation of injectable hydrogels for chronic wound healing, *J. Mater. Chem. B*, 2020, **8**(38), 8768–8780.

32 K. Zhou, X. He, Y. Liu, Z. Bei, K. Shi, D. Hu, Y. Wang, M. Gao, B. Chu, Q. Yang, C. Yang and Z. Qian, Advances in injectable hydrogel-based intra-articular treatment systems for osteoarthritis therapy, *Chin. Chem. Lett.*, 2026, **37**(3), 111723.

33 J.-k Shan, J.-q Fang, S.-H. Liu, X.-h Jin, Z.-j Weng, L.-p Nan, J.-j Liu and Y. Qian, Application and prospects of polysaccharide-based hydrogels in the treatment of intervertebral disc degeneration, *J. Mater. Chem. B*, 2025, **13**(37), 11525–11539.

34 C. Guo, L. Du, X. Du, R. Gao, X. Jiao, Z. Li, T. Zhang, P. Huang, C. Zhang, Z. Feng, W. Wang and B. Xu, ROS-responsive hydrogel loaded with berberine liposome protects against intervertebral disc degeneration by inhibiting mitochondrial fission and apoptosis, *Chem. Eng. J.*, 2025, **522**, 167108.

35 S. Yu, S. Chen, T. Tong, Y. Yan and Q. Shuai, pH and ROS Dual-Responsive Core-Cross-Linked Micelles Based on Boronic Ester Linkage for Efficient PTX Delivery, *J. Polym. Sci.*, 2025, **63**(6), 1319–1333.

36 S. Wang, Q. Fu, W. Cen, Z. Su, W. Jin, Z. Yu and S. Xu, A multifunctional hydrogel based on Sanghuang polysaccharides and MXene for infected wound healing, *Chem. Eng. J.*, 2025, **505**, 159563.

37 X. Cui, L. Wang, X. Gao, J. Wu, T. Hu, J. Zhang, X. Zhou, K.-Q. Zhang and L. Cheng, Self-assembled silk fibroin injectable hydrogels based on layered double hydroxides for spinal cord injury repair, *Matter*, 2024, 7(2), 620–639.
38 L. Li, Z. Zhao, Y. Gao, X. Jiang, H. Liu, X. Guo, X. Huang, L. Zhou, C. Liu and X.-C. Shen, Dynamic Metal-Phenolic Coordinated Hydrogel for Synergistic Photothermal/Chemodynamic Therapy against Biofilm-Infected Wounds and Real-Time Monitoring, *ACS Appl. Mater. Interfaces*, 2025, **17**(40), 56017–56039.
39 Y. Han, J. Cao, M. Li, P. Ding, Y. Yang, O. V. Okoro, Y. Sun, G. Jiang, A. Shavandi and L. Nie, Fabrication and characteristics of multifunctional hydrogel dressings using dopamine modified hyaluronic acid and phenylboronic acid modified chitosan, *Front. Chem.*, 2024, **12**, 1402870.
40 Z. Liu, J. Mao, W. Li, C. Xu, A. Lao, A. Shin, J. Wu, A. Gu, Z. Zhang and L. Mao, Smart glucose-responsive hydrogel with ROS scavenging and homeostasis regulating properties for diabetic bone regeneration, *Chem. Eng. J.*, 2024, **497**, 154433.
41 S. Li, J. Li, J. Xing, L. Li, L. Wang and C. Wang, Development and Characterization of Hyaluronic Acid Graft-Modified Polydopamine Nanoparticles for Antibacterial Studies, *Polymers*, 2025, **17**(2), 162.
42 N. Roas-Escalona, F. Becquart, T. Delair and F. Dutertre, Chitosan-based hydrogels: Influence of crosslinking strategy on rheological properties, *Carbohydr. Polym.*, 2024, **341**, 122329.
43 Y. Ge, M. Wang, Y. Zhou, Q. Pan, M. Duan, X. Zhang, R. Wang, Y. Huo, Y. Guo and W. Shen, Borate ester-crosslinked polysaccharide hydrogel reinforced by proanthocyanidins for oral ulcer therapy, *Colloids Surf., B*, 2025, **249**, 114535.
44 J. Zhang, Z. Wang, X. Lin, X. Gao, Q. Wang, R. Huang, Y. Ruan, H. Xu, L. Tian and C. Ling, Mn− Ce Symbiosis: Nanozymes with Multiple Active Sites Facilitate Scavenging of Reactive Oxygen Species (ROS) Based on Electron Transfer and Confinement Anchoring, *Angew. Chem., Int. Ed.*, 2025, **64**(4), e202416686.
45 F. Liu, G. Li, Z. An, S. Wang, S. Xu and H. Liu, Dynamic Boronate Ester Based Hydrogel with Enhanced Mechanical Properties and Multi-Stimuli-Triggered Release for Tissue Repair and Antioxidant Therapy, *Gels*, 2025, **11**(5), 370.
46 Y. Sun, J. Zhang, Y. Gu, T. Liu and L. Chen, Biomineralized mnO2 nanoparticle-constituted hydrogels promote spinal cord injury repair by modulating redox microenvironment and inhibiting ferroptosis, *Pharmaceutics*, 2024, **16**(8), 1057.
47 L. R. Chen, Y. M. Zou, R. T. Li, X. Zhou, Y. H. Lai, J. X. Chen and J. Yang, The Hybrid of Cu–TCPP@ Mn3O4 for Inflammation Relief by ROS Scavenging and O2 Production: An Efficient Strategy for Antiviral Therapy, *Small*, 2024, **20**(10), 2306095.
48 M. Kim, J. An, S.-A. Shin, S. Y. Moon, M. Kim, S. Choi, H. Kim, K.-H. Phi, J. H. Lee, U. J. Youn, H. H. Park and C. S. Lee, Anti-inflammatory effects of TP1 in LPS-induced Raw264.7 macrophages, Applied, *Biol. Chem.*, 2024, **67**(1), 16.
49 J. Li, H. Ke, X. Lei, J. Zhang, Z. Wen, Z. Xiao, H. Chen, J. Yao, X. Wang and Z. Wei, Controlled-release hydrogel loaded with magnesium-based nanoflowers synergize immunomodulation and cartilage regeneration in tendon-bone healing, *Bioact. Mater.*, 2024, **36**, 62.
50 H. Kim, T. Kim, K. A. Rahaman, J. Kwon, J.-Y. Lee, S. Cho, S. Chung, H.-S. Han and Y.-C. Kim, Synergistic Effects of Magnesium and Zinc Ions on Neural Stem Cell Proliferation and Differentiation, *JOM*, 2025, 1–12.
51 Q. Su, J. Wang, Y. Song, Z. Zhang, B. Cai, X. Xiaohalati, J. Liu, H. Li, Z. Wang and J. Chang, Bioactive Silk Sericin/Bioceramic Nerve Guidance Conduit for Effective Repair of Long-Gap Transected Peripheral Nerve Injury through Regulating Schwann Cells, Advanced, *Science*, 2025, **12**(38), e07241.
52 X. Zheng, J. Yang, Y. Hou, X. Shi and K. Liu, Prediction of clinical progression in nervous system diseases: plasma glial fibrillary acidic protein (GFAP), *Eur. J. Med. Res.*, 2024, **29**(1), 51.
53 A. K. Kanakis, I. S. Benetos, D. S. Evangelopoulos, J. Vlamis, E. S. Vasiliadis, A. Kotroni, S. G. Pneumaticos, A. Kanakis and E. Vasiliadis, Electrical stimulation and motor function rehabilitation in spinal cord injury: a systematic review, *Cureus*, 2024, **16**(5), e61436.
54 Y. Li, Y. Gu, Z. Wang, Y. Wang, S. Jiang, K. Wang, Y. Zheng, R. Feng and M. Yang, GelMA Hydrogel Encapsulating iPSC-Derived Human Spinal Cord Organoids Enhances Neural Regeneration and Restores Motor Function in Rat Spinal Cord Injury, *J. Biomed. Mater. Res., Part A*, 2025, **113**(10), e38001.
55 D. J. DiSabato, C. M. Marion, K. A. Mifflin, A. N. Alfredo, K. A. Rodgers, K. A. Kigerl, P. G. Popovich and D. M. McTigue, System failure: Systemic inflammation following spinal cord injury, *Eur. J. Immunol.*, 2024, **54**(1), 2250274.
56 Y. Wang, C. Chen, C. He, W. Dong, X. Yang, Q. Kong, B. Yan and J. He, Quaternized chitosan-based biomimetic nanozyme hydrogels with ROS scavenging, oxygen generating, and antibacterial capabilities for diabetic wound repair, *Carbohydr. Polym.*, 2025, **348**, 122865.
57 A. Nassar, S. Hegde, D. Chandran, S. Pahadasingh, A. Nayak, S. Satarker, P. C. Gurram, D. Upadhya and M. Nampoothiri, Pharmacological inhibition of RE1 silencing transcription factor disrupts SOX2 expression and neurogenesis in human induced pluripotent stem cells derived neuronal models, *Metab. Brain Dis.*, 2025, **40**(8), 318.
58 M. Danen, Assessment of Peripheral Nerve Regeneration Across a 7 mm gap in the Delayed Rat Median Nerve Model: A Comparative Study of Autologous Nerve Graft, Muscle Filled-in Vein Conduit, and Extracellular Vesicle-Based Therapies, Technische Universität Wien, 2025.
59 F. Shao, X. Sun, Q. Yu, K. Wang, C. Sun, Q. Wang, X. Cao, L. Zhang, P. Fu and X. Yang, Lycium barbarum oligosaccharide-derived carbon quantum dots inhibit glial scar formation while promoting neuronal differentiation of neural stem cells, *Int. J. Biol. Macromol.*, 2024, **282**, 137474.